To the Graduate Council:

I am submitting herewith a thesis written by Paul A. Jalbert entitled "Development of a Hybrid Probe for Gas Turbine Combustor Measurements." I have examined the final copy of this thesis for form and content and recommend that it be accepted in partial fulfillment of the requirements for the degree of Master of Science, with a major in Mechanical Engineering.

Roy J. Schulz

Dr. Roy J. Schulz, Major Professor

We have read this thesis
and recommend its acceptance.

Accepted for the Council:

DEVELOPMENT OF A HYBRID PROBE
FOR GAS TURBINE COMBUSTOR MEASUREMENTS

A Thesis

Presented for the

Master of Science

Degree

The University of Tennessee, Knoxville

Paul Armand Jalbert

December 1997

DEDICATION

This thesis is dedicated to my wife, Cynthia, and my son, Stephen.

ACKNOWLEDGMENTS

I would like to acknowledge the efforts of several Sverdrup colleagues who contributed to the successful development of the prototype hybrid probe. Robert S. (Bob) Hiers, Jr. provided the leadership required to bring together skills in high temperature probe design, optical system design, and prototype system fabrication. Celia A. Doub, provided the optical system design. Michael D. McClure provided the NPARC computational fluid dynamic solutions. Daniel G. Brown provided the SSIRM code solution.

I would also like to acknowledge the United States Air Force and Sverdrup Technology, Inc., AEDC Group for funding my graduate studies at the University of Tennessee Space Institute. Development of a hybrid probe system for diagnostic measurements at the exit plane of a prototype combustor was a funded task in FY97 (Job 1916, Intrusive Diagnostics) at the Arnold Engineering Development Center (AEDC), Arnold Air Force Base, TN. This thesis has been approved for public release and the distribution is unlimited.

The work reported herein was conducted at the Arnold Engineering Development Center (AEDC), Air Force Materiel Command (AFMC). The results were obtained by Sverdrup Technology, Inc., AEDC Group, operating contractor for the propulsion test facilities at AEDC, AFMC, Arnold Air Station, Tennessee, under Job 1916. The Air Force Project Manager was Capt. Andrew C. Walton. The manuscript was submitted for publication on December 1, 1997.

ABSTRACT

An innovative approach has been used to provide optical access to a combustor exhaust flow for nonintrusive measurements in the high temperature flow. This hybrid probe system combines a line-of-sight optical measurement system with an intrusive, high temperature - capable probe for emission, absorption, or transmission spectral measurements in the high temperature flow.

A single 0.94 inch diameter probe concept was selected to be compatible with existing pitot / emission combustor exit rakes and to avoid the significant design challenge of maintaining optical alignment across long path lengths. The optical components were positioned at the top and bottom of a 0.25 inch flow-through slot and protected by a rearward facing step and a local circumferential air purge flow. The optical components housed inside the probe included two sets of lenses and fiber optic cables. The probe was designed for easy installation and removal of the optical assemblies from each end of the probe.

Water cooling passages running longitudinally within 0.050-inch from the surface provided a thermal barrier for the optical components. A hydraulic and thermal analysis of the probe identified the water flow rate required to maintain the probe surface temperature at 1200 °F.

The aerodynamic shape of the flow-through slot in the probe was designed so that the gas properties at the optical line of sight were minimally disturbed from free stream conditions. A numerical solution of the flow field through the slot predicted a maximum

density change from the free stream density of less than 1.0 percent and a Mach number change of 0.05.

The first application of the hybrid probe was to obtain transmission measurements of a continuum light source in a natural gas / air combustor exhaust at 200 psia and 3000 °F. The source fiber optic cable was severed during installation prior to the test and no optical transmission data were obtained. However, probe durability was satisfactory with no signs of external thermal distress. The use of purged orifices as windows to protect the internal optical components of the probe from damage or contamination was successful.

The presence of the hybrid probe was shown to have a negligible effect on flow conditions at the optical path of the transmitted beam - a necessary condition for directly inferring free-stream conditions from hybrid probe measurements. The hybrid probe was also shown to be dimensionally stable since the optical alignment repeated pre- and post-test.

TABLE OF CONTENTS

LIST OF TABLES

LIST OF FIGURES

1.0 INTRODUCTION

The design of combustors for modern, state-of-the-art gas turbine engines is primarily concerned with three objectives: 1) maximum combustion efficiency, 2) economical operation, and 3) compliance with regulatory limits on exhaust gas pollutants. During development testing of a prototype combustor, gas measurements made at the combustor exit include static pressure, pitot pressure, stagnation temperature, and species concentration (e.g. [CO_2], [CO], unburned fuel [HC], [NO], [NOx], and [O_2]) and particulate or smoke.

Nonintrusive optical emission / absorption techniques provide fast response gas measurements without altering the flow properties. These techniques require clear optical access to the flow for transmission of a continuum radiation light source in the ultraviolet (UV), infrared (IR) and visible wavelength spectrum. When optical access to the flow is not available, flow property measurements are facilitated by probes positioned in the flow. The presence of the probe, especially the extractive tubing, alters the properties of the flow and provides an averaged measurement with relatively slow time response.

A method of providing optical access to a combustor exit flow is required to facilitate optical measurement of the thermodynamic properties of the chemically reacting combustion gas. The goal of this work is to develop a minimally intrusive "hybrid" probe system that will provide optical diagnostic measurements of high temperature, high velocity flows that are generally inaccessible to optical diagnostic techniques.

A hybrid probe is an optical measurement system packaged in a probe positioned in or adjacent to a flowing gas. The presence of the probe has a minimal affect on the flow providing a clear optical path for radiation transmission measurements. Development of the proposed hybrid probe system is expected to result in an improved method for measuring the gas properties at the exit of a gas turbine engine combustor. The feasibility of this technique depends on probe structural integrity (durability and optical alignment).

Previous Experience

Optical probe systems have been used for many years for internal engine diagnostic measurements. During the late 1960's pyrometer probes were developed to measure the surface temperatures of aircraft turbine blades during operation. The first optical systems employed simple lenses to focus radiation energy from high temperature turbine blades onto a detector mounted on the engine case. Fiber optic cables were used to transmit the signal to a detector in a benign location. During the 1970's traversing pyrometer probes were developed to provide three dimensional surface temperature maps [1][1].

Development of pyrometry probes continues in the 1990's with a focus on laser excitation of thermographic phosphors. Miniaturization of optical fibers allows bundles of fused silica fibers (source and detector optics) to be contained in a single probe. Air-cooling maintains the probe structural integrity and also purges the sapphire lens [2].

An optical probe system was developed to survey a small ethylene / air turbulent flame with a helium neon (HeNe) laser to measure the soot volume fraction by absorption and temperature by two-color pyrometry. Two water cooled probes were positioned near the flame, one housing the source optics and the other supporting the detector optics. The spatial separation of the two probes was 5 mm. The influence of the presence of this

[1] Numbers in brackets identify references which are located on pages 28 and 29.

probe system was considered to be negligible by comparisons of the probe results with nonintrusive measurements in this symmetrical flame [3].

Advances in fabrication techniques have been incorporated into optical probe designs. New methods of bonding sapphire to high-temperature capable metals have extended the temperature range of uncooled probes to 1100°F and beyond 5000 psia [4].

An insertion type probe has been developed to aid in the understanding and reduction in the infrared (IR) signatures of jet aircraft engines. The probe scans the internal surfaces of a jet engine exhaust nozzle for the presence of hot spots and non-functional film or slot-cooling sections. The probe inserts from the engine exit to position a periscope - type rotating optical head with an IR sensor. The air film - cooled probe is mounted on a water cooled probe pusher mechanism [5].

Only Coppalle and Joyeux [3] provided experience with separate probes for the source and detector optics. But their application was limited to a laboratory small scale burner. Aeromet, Inc. has developed a flight - worthy forward scattering spectrometer probe (FSSP), the primary instrument for measuring small ice particles and water droplets in the atmosphere. The measurement is based on the in-situ scattering of a light directed from a source in one arm to a detector in another arm of the same assembly [6]. Although the measurement conditions are not thermally severe, this design alleviates the optical alignment problems associated with long optical path lengths in a dynamic environment.

High temperature probes have been developed at AEDC for measurement of temperature, pressure and species concentration in very high temperature environments.

The durability of these probes depends on water - cooled assemblies of stainless steel (Figure 1[2], [7]). These probes have been used for gas turbine engine exit measurements, hypersonic test facility calibrations, combustor development tests and to validate nonintrusive measurements of the same parameters [8].

Concept Selection

The baseline concept for a hybrid probe combustor diagnostic tool assumed that the prototype system would make a qualitative particulate assessment of the flow by transmission of a continuum source. An initial conceptual system was modeled after the laboratory success of Coppalle and Joyeux with two probes positioned on opposite sides of the combustor exit duct (Figure 2a). However, maintaining optical alignment across a 5 inch by 12 inch duct with high dynamic loads was considered to be high risk. An innovative approach was conceived based on a successful pitot / emission probe design (Figure 1) which spanned a single probe across the flow. A slot in the probe guided the flow passed the source and detector optics positioned in the top and bottom center of the slot (Figures 2b and 2c).

The technical challenges faced in this hybrid probe development are:

1. The slot inlet radius of curvature will be selected to minimize acceleration of the flow through the slot in the vicinity of the optical line of sight without increasing the stagnation point convective heating.
2. Structural integrity of the probe will be maintained by an active cooling system. The probe metal temperature will be controlled to preserve optical alignment and

[2] All tables and figures are contained in Appendix A.

keep the optical components within their operational limits.

3. The optical components must be kept free of soot. A rearward facing step ahead of the optical line of sight will guide the flow over the optics. A purge flow around the optics will be applied to remove any particulate that may be trapped in the eddy behind the step.

2.0 PROBE DESIGN REQUIREMENTS

Gas Properties

The design requirements for the hybrid probe are based on measured gas properties in the exhaust flow of a hydrocarbon fueled combustor including mass flow rate, static and stagnation pressure and the gas composition. The measured gas composition included the mole fractions of oxygen, $[O_2]$, carbon dioxide, $[CO_2]$, carbon monoxide, $[CO]$, nitric oxide, $[NO]$, the oxides of nitrogen $[NO_x]$, and unburned hydrocarbons $[HC]$. In order to calculate the heat flux from the gas to the probe several other flow parameters are required.

The Society of Automotive Engineers (SAE) aerospace recommended practice for calculating combustion gas properties [9] was used to derive the water vapor mole fraction, H_2O, and the nitrogen mole fraction, N_2. This procedure uses a matrix solution of the set of molecular balance equations (O, N, H, C) for the chemical equation for combustion of a hydrocarbon fuel in wet air (Appendix B).

$$
\begin{aligned}
&C_M H_N + X\left[R[O2] + S[N2] + T[CO2] + SPHUM1[H2O]\right] = \\
&P1[CO2] + P2[N2] + P3[O2] + P4[H2O] + P5[CO] + P6[C_X H_Y] + P7[NO2] + P8[NO]
\end{aligned}
$$

The calculated mole fractions that balance the combustion equation were used to calculate the thermodynamic properties: gas molecular weight, specific heat at constant pressure, gas constant, and the ratio of specific heats. These calculated parameters combined with the measured combustor exit static and stagnation pressures and total mass flow rate yield Mach number, velocity, density, and the adiabatic flame temperature.

Convective heat transfer calculations require absolute viscosity, thermal conductivity, Reynolds number, Prandtl number. The Thermodynamic Equilibrium Program (TEP™, [10]) was used to calculate these properties for the combustor exhaust gas. This personal computer (PC) software solves a variety of chemical gas equilibrium problems. In this case the scramjet problem solver was used. Natural gas ($C_{1.031}H_{4.17}$) and wet inlet air were specified along with the combustion chamber static pressure and temperature and the oxidizer-to-fuel ratio. The combustor exit velocity was specified so that the scramjet problem solver would give a subsonic solution. The measured and predicted combustor exhaust gas properties are summarized in Table 1. Confidence in the TEP™ solution is demonstrated by comparing the measured and predicted products of combustion, within ± 3.3 percent.

The convective heat transfer calculations also require Reynolds number, Prandtl number and thermal conductivity of the gas evaluated at the specified probe surface (TSURF = 1200°F). TEP™ was used to evaluate these parameters over the temperature range from 1000°R to 3500 °R (Figure 3).

<u>Duct Geometry</u>

The geometry of the duct where the prototype probe design validation testing occurred is presented in Figure 4. The duct is a converging S-duct. The hybrid probe replaced the fifth of the seven pitot / sampling rakes two inches upstream of the duct exit. The size of the prototype hybrid probe was dictated by existing accommodations in the boilerplate rig for the pitot / emissions probes. The maximum probe diameter was 1.0 inch and the probe must span the 4.8 inch duct.

3.0 PROBE THERMAL DESIGN

Probe Heating Load Analysis

The heating load on the probe in the combustor exhaust duct consists of the convection heating, radiation heating, and gaseous emission heating. Knowledge of the heating load distribution over the probe surface is required to match the cooling water distribution with the heating distribution. Normally, cooling water flow distributed evenly around the probe creates a thermal barrier to maintain structural integrity. Since optical misalignment will result from non-uniform thermal deformation of the probe structure, more care was taken to balance the water flow rates in the probe cooling water passages with the heating load distribution on the surface of the probe. The heating load calculation was done as a conservative engineering analysis because of the relatively high uncertainty (± 25 percent) in heat transfer coefficients.

Convection Heating Load

The prototype hybrid probe will be tested in a rectangular duct in a row with six pitot / emission probes. The duct blockage due to the seven one inch diameter probes is 52 percent causing the flow accelerate from a Mach number of 0.20 to 0.47. Three options were considered for the convective heating thermal model, a single probe in the flow at a Mach number of 0.20, a single probe in the flow at a Mach number of 0.47, and a single row of seven probes at a Mach number of 0.47. The literature offers several choices for the temperature differential that drives the heat transfer. In low speed flow either $(T_{wall} - T_{gas})$ or $(T_{wall} - T_{film})$ have been used [11]. As the flow velocity increases $(T_{wall} - T_{adiabatic\ wall})$ is required [12]. In flow across banks of tubes in a crossflow

(T_{wall} - $T_{arithmetic\ mean}$) is required [11]. The average convective heat flux to the hybrid probe for each of these three options, considering the large uncertainties in the heat transfer coefficients, was approximately 200 $^{BTU}/_{ft2\text{-}sec}$ (Figure 5). Therefore, the simplest model, the single probe in the flow at a Mach number of 0.20, was selected for the convective heating load analysis.

The average convective heating load was calculated from the equation:

$$q_c = \bar{h} \times A_s \times (T_s - T_\infty)$$

where: $\bar{h} = \dfrac{\overline{\mathrm{Nu}_D} \times k}{D}$, film coefficient, $^{BTU}/_{ft\text{-}s\text{-}°R}$

$\overline{Nu_D}$ = Nusselt number

A_s = probe surface area, ft^2

T_s = probe surface temperature, °R

T_∞ = gas static temperature, °R

k = gas thermal conductivity, $^{lbf}/_{sec\text{-}°R}$

D = probe diameter, ft

Three equations were selected for use in finding an average Nusselt number, $\overline{Nu_D}$ [11]. All were based on empirical data over specific ranges of Reynolds number and Prandtl number. These particular equations were selected because there was a good match on the Reynolds number and Prandtl number range of application.

$$\overline{Nu_D} = C \times \mathrm{Re}_D{}^m \times \mathrm{Pr}^n \times \left(\frac{\mathrm{Pr}}{\mathrm{Pr}_s}\right)^{\frac{1}{2}} \qquad \text{(Zhukauskas, [11])}$$

with all parameters except Pr_s evaluated at T_∞

where: $C = 0.26$ for $10^3 \le Re_D \le 2x10^5$

$m = 0.26$ for $10^3 \le Re_D \le 2x10^5$

$n = 0.37$ for $Pr \le 10$

Pr_s = Prandtl number evaluated at the probe surface temperature, T_s

$$\overline{Nu_D} = 0.3 + \frac{0.62 \times Re_{Df}^{\frac{1}{2}} \times Pr_f^{\frac{1}{3}}}{\left(1+\left(\frac{0.4}{Pr_f}\right)^{\frac{2}{3}}\right)^{\frac{1}{4}}} \times \left(1+\left(\frac{Re_{Df}}{282,000}\right)^{\frac{5}{8}}\right)^{\frac{4}{5}} \qquad \text{(Churchill and Burnstein, [11])}$$

with all properties evaluated at the film temperature, $T_f = \frac{1}{2} \times (T_s + T_\infty)$.

$$\overline{Nu_D} = C \times Re_{Df}^{\ m} \times Pr_f^{\frac{1}{3}} \qquad \text{(Hilpert, [11])}$$

with all properties evaluated at the film temperature, $T_f = \frac{1}{2} \times (T_s + T_\infty)$

where: $C = 0.027$ for $4x10^4 \le Re_D \le 4x10^5$

$m = 0.805$ for $4x10^4 \le Re_D \le 4x10^5$

Pr_f = Prandtl number evaluated at the film temperature

The Nusselt numbers calculated from the three methods were 302.27 from Zhukauskas [11], 422.41 from Churchill and Burnstein [11], and 550.02 from Hilpert [11]. The average of the three Nusselt numbers was 424.9 with a quoted uncertainty of ± 25 %. The average film coefficient was calculated to be 0.1008 $^{BTU}/_{ft2\text{-}sec\text{-}°R}$. The total convective heating load to the probe was 16.85 $^{BTU}/_{sec}$.

The convective heating distribution around the probe was derived from local Nusselt number data for airflow normal to a circular cylinder [11]. The data from Reynolds numbers of $1.7x10^5$ and $1.4x10^5$ were interpolated to find a Nusselt number versus probe angle for design Reynolds number, Re_D = 158,341. The average Nusselt number for the interpolated Reynolds number was 406. The final Nusselt number curve was achieved by adjusting the curve upward by the ratio of 424.9 / 406. Figure 6 presents the Nusselt number distribution over the surface of the hybrid probe.

<u>Radiation Heating Load</u>

The radiation heating load on the probe was estimated for a uniform probe surface temperature, T_{SURF}= 1200°F, and a black body with a temperature, T_{BB}, of 1600°F:

$$q_R = A_{PROBE} \times \sigma \times \left(T_{BB}{}^4 - T_{SURF}{}^4\right)$$

where: $\sigma = 0.1714\ ^{BTU}/_{hr\text{-}ft^2\text{-}°R^4}$

The total radiation heating load on the total probe surface was calculated to be 0.487 $^{BTU}/_{sec}$. The black body approximation for the radiation heating load on the probe was used rather than the more rigorous shape factor approach for two reasons. First, due to 'S" curve in the duct, the probe sees nothing but hot carbon steel walls. Second, the precise temperature distribution along the uncooled duct walls is unknown.

<u>Gaseous Emission Heating Load</u>

The products of combustion contain approximately ten percent water vapor and four percent carbon dioxide at a gas temperature of 3359 °R so the heat transfer to the probe from gaseous emissions is significant. The heat load from gaseous emissions was calculated from the equation:

$$q_e = \varepsilon_g \times A_s \times \sigma \times T_\infty^4$$

Initially, the emissivity of the gas, ε_g, was calculated using the empirical relations in [11]. The mean beam length L_e for probe surface area A_S in duct volume V_{DUCT} of arbitrary shape is

$$L_e = 3.6 \times \frac{V_{DUCT}}{A_S} = 1.718 \text{ meters.}$$

The static pressure in the duct is 184.4 psia and the partial pressures for carbon dioxide and water vapor are 7.28 psia and 18.35 psia, respectively. The emissivities of carbon dioxide and water vapor were estimated to be 0.154 and 0.378, respectively. The emissivity of the combined gases was estimated to be 0.472. However, the pressure correction terms for the carbon dioxide, water vapor, and combined gas emissivities at the high duct static pressure required large extrapolations of the empirical data. For this reason, an additional approach was considered. The Standardized Infrared Radiation Model, (SIRRM, [13]) was used. The SIRRM code returns a gaseous emissivity

$$\bar{\varepsilon} = \frac{\int N_{BB} \times \varepsilon_\lambda \times d\lambda}{\int N_{BB} \times d\lambda} = \frac{8.68 \dfrac{W}{cm^2 - sr}}{21.88 \dfrac{W}{cm^2 - sr}} = 0.397$$

which is the combined water vapor - carbon dioxide spectral emissivity divided by the Planck's function at the gas temperature of 3359 °R. Agreement between the two emissivities was within 16 percent but the SIRRM code value was used. The total heat load to the probe surface from gaseous emissions was calculated to be 2.366 $^{BTU}/_{sec}$.

Total Heating Load Distribution

The total heating to the probe surface is the sum of the convective, radiation, and gaseous emission heating loads. The total heating load on the probe was 19.929 $^{BTU}/_{sec}$. Radiation and gaseous emission heating is distributed uniformly over the probe surface. Convective heating varies with the Nusselt number around the probe. The total heating load distribution over the probe is presented as a function of angle from the flow in Figure 7.

Heating Load to the Slot Walls

The convective heating load to the slot side walls was modeled as turbulent flow over a flat plate. The average Nusselt number was calculated from:

$$\overline{Nu_x} = 0.0296 \times Re_x^{\frac{4}{5}} \times Pr^{\frac{1}{3}} \qquad \text{(Chilton - Colburn, [11])}$$

The average Nusselt number was 362.78. The average film coefficient was 0.092 $^{BTU}/_{ft2\text{-}sec\text{-}°R}$ and the total convective heating load to each side wall was 1.436 $^{BTU}/_{sec}$. . The slot wall heating load calculations are contained in Appendix C. The gaseous emission heating load was considered negligible due to the small surface area involved. The radiation heating load was considered negligible due to the small view factor involved.

Hydraulic Calculations

A model of the probe cooling system was assembled using an EXCEL™ spreadsheet [14]. The model included the facility water supply and return tubing and the ten individual flow paths connecting the probe supply manifold to the return manifold (Figure 8). The hydraulic calculation methodology is summarized in Appendix D. A preliminary estimate of the water flow rate, MDOTW, versus the square root of the difference in water supply and discharge pressures ($(PS - PB)^{1/2}$, Figure 9) was used in the hydraulic calculations. The preliminary water flow rate estimate was based on data recorded during flow checks of a water cooled pitot / emissions probe of similar design [7]. The water supply temperature, TS, was assumed to be constant at 70°F for the open loop cooling water system.

Since the actual water flow rate through the probe is controlled by the system back pressure, a maximum back pressure of 100 psia was assumed. The pressure losses in the probe return tubing were calculated, added to the maximum back pressure, and assumed to be the minimum return manifold water pressure. The pressure in the return manifold must exceed this minimum pressure or the water flow rate will be reduced below the preliminary total flow rate estimate.

The minor losses in each water flow path, A - J, were estimated including entrance losses, elbow losses (E and F only), flow path friction losses, and sudden expansion losses. The flow path entrances at the supply and turn around manifolds were considered to be sharp edged. The flow paths were considered to be smooth pipes. The sudden expansions at the turn around and return manifolds were estimated based on the ratio of the flow path and the local manifold effective diameter. The elbows were considered to be short radius elbows [15].

Once the hydraulic model was assembled in the spreadsheet, a first estimate of the water flow rate through each flow path, MDOT1X, was made such that the sum of the rates, MDOT1X equaled the total flow rate, MDOTW, for the given $(PS - PB)^{1/2}$. The water pressure in the turn around manifold, PTM, was calculated based on the first flow rate assumption. Then, using the EXCEL™ "GOALSEEK" function, the turn around manifold pressure was iterated until the sum of the ten flow path flow rates equaled the total probe flow rate within ± 0.5 %.

The water flow rate through each supply flow path, MDOT1X, was used as a first estimate for the flow rate through each return flow path, MDOT4X. Again, using the EXCEL™ "GOALSEEK" function, the return manifold pressure, PRM, was iterated until the sum of the ten return flow path flow rates equaled the total return water flow rate, MDOTW.

The predicted water pressure loss through the probe system is presented in Figure 10. The output of the pressure loss model was used as the input for the cooling efficiency model. The dimensions, water mass flow rate, and Reynolds number for each flow path were linked to another EXCEL™ spreadsheet containing the cooling efficiency model. This model was used to determine the total heat removed from the probe by the cooling water.

The Nusselt number for the water flow was calculated using the Dittus-Boelter equation for turbulent flow in circular tubes with heating [11].

$$\overline{Nu_D} = 0.023 \times Re_D^{\frac{4}{5}} \times Pr^{\frac{2}{5}}$$
$$0.7 \le Pr \le 160$$
$$Re_D \ge 10^4$$
$$\frac{L}{D} \ge 10$$

A one-dimensional energy balance from the probe surface to each water flow path was solved to obtain the cooling water temperature increase (Appendix E). A segment of the probe surface area and a maximum metal path length were assigned to each flow path (Figure 11). The wall temperature of each flow path was calculated from

$$TFPWALLX = \frac{\left(\frac{KSSTL \times ASURFX \times TSURF \times 12}{LMX} + HW1X \times PX \times TS\right)}{\frac{KSSTL \times ASURFX \times 12}{LMX} + HW1X \times PX}$$

and the cooling water temperature increase in each flow path was calculated from

$$TFPWATERX = \frac{QDOTFPX}{MDOT1X \times CPW} + TTM$$

The water temperature in the turn around manifold, TTM, was calculated from an energy balance of each of the supply flow paths and used in the pressure loss calculations and the cooling efficiency calculations for the return flow paths. The water temperature increase across the probe is plotted in Figure 12 for a range of water supply pressures.

Review of the probe cooling results shows that the average flow path wall temperature increases as the water flow rate decreases. This is as expected because heat transfer to the cooling water is greater at lower water velocities. Figure 12 shows that the slower water heats more quickly and the temperature difference between the water and the probe surface is reduced. The net result is the average probe structure temperature approaches the design probe surface temperature as the cooling water flow rate is reduced.

The affect of cooling water flow rate on optical alignment was assessed by calculating the difference between the supply and return wall temperatures for each flow path, A- J. Figure 13 plots this temperature difference for each flow path for cooling water flow rates from 1.78 to 2.97 gpm. The average flow path wall temperature increases from 1146°F at the maximum water flow rate to 1163°F at the minimum water flow rate. At the maximum and minimum water flow rates, the flow path wall temperature differences are half of the temperature differences at the intermediate water flow rates. The maximum temperature differences are approximately 20°F and occur in the vicinity of the slot. The thermal deformation across the slot is calculated from

$$\Delta = \alpha \times \delta T \times L$$

where Δ = linear deformation , in.

α = coefficient of thermal expansion, 6.5 $\times 10^{-6}$ in/in-°F

δT = supply flow path minus return flow path wall temperature difference,°F

L = length of the flow-through slot, 1.76 in.

For the 20°F temperature difference, the thermal deformation of 2.2×10^{-4} in. corresponds to and angular misalignment of 7.16×10^{-3} degrees or 0.43 minutes. The spherical optics used on the prototype hybrid probe optics can tolerate up to 1 degree of misalignment [16].

4.0 PROBE AERODYNAMIC DESIGN

Success of the hybrid probe design depends on the flow through the slot remaining unchanged from the free stream conditions. The inlet radius of curvature on the slot walls was selected to avoid accelerating the flow in the slot without drastically increasing the stagnation point heat transfer. The width of the slot was sized such that the boundary layer build-up on either side of the slot would not reach the slot centerline. The rearward facing step was sized such that the flow would not reattach upstream of the optical line of sight. The effect of the slot corners on the flow through the slot was unknown. An assessment of the flow quality in the slot was required both at the design conditions and the off-design conditions.

On-Design Performance

A numerical model of the hybrid probe was used to select the best inlet radius of curvature on the slot walls and to predict the properties of the flow in the slot. At the request of the author, Michael A. McClure, Sverdrup Technology, Inc., AEDC Group, modeled the flow field around the probe and through the slot and provided the numerical solutions for interpretation by the author. Mr. McClure used the NPARC code, a three dimensional viscous flow solver [17]. The gas properties at the design conditions (Table 1) were used as inputs to the code. An axis-symmetric model was assembled which included three inlet radii of curvature on the horizontal and vertical edges (0.03125 inch, 0.0625 inch, and 0.125 inch), the 0.13 inch rearward facing step in the slot, and the probe exterior. The two dimensional NPARC solution for the 0.03125 inch radius of curvature predicted a Mach number at the optical line of sight of 0.250 (Figure 14) and the probe stagnation point and separation point locations, as well as gradients of Mach number, static pressure and static temperature through the slot. Also, the location of the flow reattachment point behind the rearward facing step was identified [18].

A comparison of the free stream flow properties and the flow properties at the optical line of sight is summarized below:

	Free Stream Conditions	Conditions at the Optical Line of Sight (3-D Solution)	Difference
Mach Number	0.201	0.25	0.05
Static Pressure, psia	184.4	181.9	-1.36 percent
Static Temperature, °R	3359	3346	-0.39 percent
Density, lbm/ft^3	0.1439	0.1425	-0.98 percent

The flow reattachment point occurred 0.51 inches down stream of the step and 0.38 inches downstream of the optical line of sight. This reattachment point does not account for the purge flow around the optics which is expected to add further protection of the optics.

Off-Design Performance

A water tunnel test was conducted to visually assess the complex flow through the slot in the probe to determine if the flow at the optical line of sight was perturbed by the presence of the probe at off-design conditions.

The UTSI water tunnel [19] is a horizontal, closed circuit with a plexiglass side wall in the test section which measures 30.5 cm by 45.7 cm by 150 cm long. The tunnel is powered by a 25 cm diameter two-bladed propeller which is located at the second bend downstream of the test section. The water velocity is variable up to 11 inches per second. The velocity is determined by correlating the propeller shaft speed with the water velocity previously calibrated by a hot film probe. Streak lines, lines showing the path of dye particles that passed through a single point were created by injecting fluorescent dye with a hypodermic needle. The dye was illuminated in the horizontal plane by an argon ion laser. Video data was recorded by a camera positioned above the test section. Still color photographs were also made from the open top and through the plexiglas side wall.

The actual probe body was used for the water tunnel study. At the time of the water tunnel test, the probe was partially complete, unplugged holes and open manifolds were plugged for this test. The approximate one-inch diameter base of the probe fit exactly into an existing model support in the floor of the water tunnel test section.

The maximum water tunnel Reynolds number was limited to 5,400 by the maximum water tunnel velocity of eleven inches per second and water temperature of 60°F. Even though this was considerably lower than the design Reynolds number of 158,000, the water tunnel test was useful in visualizing flow through the slot from 0 to 10 degrees water approach angle. The preliminary and strictly qualitative results of the water tunnel test are summarized below:

- Changes in the location of the flow stagnation point on either side of the middle of the slot could not be visually detected as the probe was rotated ± 10 degrees.
- The flow separated at the 100 - 110 degree point on the lee side of the probe. The location of the flow separation point confirmed the NPARC results showing no

influence of the slot on the flow separation angle from the cylindrical probe (Figure 15).

- Even at inlet flow angles up to ten degrees, the streak lines tended towards stream lines through the slot. The stream line flow persisted for almost one probe diameter down stream of the slot.
- The size of the probe made it too difficult to assess the flow over the rearward facing step ahead of the fiber optic ports in the top and bottom of the slot.
- Since the data of most interest was the presence of near-stream line flow, interpretation of the illusory vortices [20] behind the probe were of little concern.

5.0 DESIGN VALIDATION TEST RESULTS

Water flow checks were completed on the finished prototype probe and compared to the estimated water flow rates used in the hydraulic design. When the measured supply and discharge water pressures are adjusted to account for the differences in the supply and discharge tubing lengths, the actual water flow rates agree well with the preliminary estimate in the range of design flow rates (Figure 10).

The initial validation test of the prototype hybrid probe design validation testing was conducted in a full-scale combustor development test rig. The hybrid probe replaced the fifth of seven pitot emission probes (just off-centerline). The combustor rig burned natural gas and air in a test period lasting eight hours. The most severe steady state test conditions for the design validation test were essentially the same as the design conditions.

The effectiveness of the cooling water in maintaining the integrity of the probe structure and alignment of the optical components was the critical test objective. Considering the integrity of the probe itself, there was no evidence of dimension change, melting, or indications of excessive probe surface temperature. Dark deposits of combustion product condensate were found in moderate surface temperature regions and bare metal in the hotter regions. This result is typical of the emissions probes and indicates that the structural cooling of the hybrid is at least as effective as that for other probes of the same design concept.

Another indication that the probe cooling was successful was found when the probe could be completely disassembled without difficulty. All of the small locking screws were removed without undue stress or breakage. All threads were clean and free of burrs. The internal carriages that hold the optical components in alignment were also removed with ease. These internal parts exhibit no evidence of high temperature. It is therefore concluded that the probe design is successful with respect to cooling design, maintainability, and operability.

The second critical test objective was to demonstrate optical alignment as the probe was subjected to heating and cooling cycles in the combustor test rig. Unfortunately one of the fiber bundles was severed following initial installation and was not discovered until after the test. Consequently transmission between the source optics and the detector optics could not be used as a measure of maintenance of optical alignment during the test. However the alignment was examined following the test by transmitting light through the operable fiber optic. The light through this fiber bundle fell at the same spot as before the test. This pre- and post-test observation is a necessary condition that the probe optics stay aligned during a test and hence is a positive but not conclusive result. Additional tests are planned in the combustor test rig when optical alignment will be checked again.

The ability of the purge to keep the optical components clean and free of combustion product residue was another critical test objective that was successfully demonstrated during this design validation test. The internal components were examined with an electron microscope following the test. No evidence of combustion products was found on any of the internal optical or mounting components.

The final test objective to confirm that the flow at the optical line of sight was undisturbed from the free stream flow. The static pressure of the flow measured in the slot is compared with the measured duct static pressure in Figure 16. At the design free stream Mach number of 0.20, the NPARC solution predicted a slot Mach number of 0.25 in the slot at the optical line of sight. Recall that the NPARC solution was for a single probe in the flow. The Mach number corresponding to the measured slot static pressure of 169.7 psia is 0.47 which precisely matches the Mach number of the flow at the minimum area between the seven probes. Even though the flow around the hybrid probe was accelerated, the pressure of the flow in the slot matched the local conditions. This implies that when the flow is not accelerated around the probe (i.e. when the hybrid probe alone is used) the flow through the slot will remain unchanged from the free stream conditions.

6.0 CONCLUSIONS AND RECOMMENDATIONS

An innovative approach has been used to provide optical access to combustor flow paths. A single probe that spans the duct has been designed which contains the optical components required for emission, absorption, or transmission measurements in the high temperature flow. The aerodynamic and thermal design concepts employed on previously validated pitot / sampling probes have resulted in a hybrid probe with demonstrated durability and operability in turbine engine combustors.

The hybrid probe has been shown to have negligible effect on flow conditions in the optical path of the transmitted beam - a necessary condition for directly inferring free-stream conditions from hybrid probe measurements. The hybrid probe was also shown to be dimensionally stable since the optical alignment repeated pre- and post-test.

The use of purged orifices as windows to protect the internal optical components of the probe from damage or contamination caused by combustion gas has been demonstrated to be completely satisfactory.

The only remaining feature to be demonstrated before the hybrid probe can be transitioned for use as an operational probe for specific applications is the invariance of the optical alignment as the probe is thermally cycled in the combustion gas. This is the final design validation test planned for the hybrid probe since the probe has satisfied all other design requirements.

This hybrid probe concept has many potential applications including an emission / absorption measurement for nitric oxide, a transmission measurement to quantify particulate (soot) in the flow, and a visible light endoscope probe to measure clearances within an operating combustor. Continued development of this hybrid probe concept will focus on the use of improved optics to maximize light through-put, miniaturization of the probe cross section and simplification of the manufacturing process.

REFERENCES

1. Atkinson, W.H. and R.R. Strange, "Turbine Pyrometry for Advanced Engines," AIAA Paper 87-2011, July, 1987.

2. Alaruri, S., D. McFarland, A. Brewington, M. Thomas, and N. Sallee, "Development of a Fiber-Optic Probe for Thermographic Phosphor Measurements in Turbine Engines," AIAA Paper 94-2987, June, 1994.

3. A. Coppalle and D. Joyeux, Temperature and Soot Volume Fraction in Turbulent Diffusion Flames: Measurements of Mean and Fluctuating Values, *Combustion and Flame*, 96:275-285, 1994

4. Cushing, F.S., "New Developments in F-O Sensor Probe Design", *SENSORS®, The Journal of Applied Sensing Technology*, Vol. 11, No. 9, pages 49 - 54, Helmers Publishing, Inc., Peterborough, NH, September, 1994.

5. McCullough , R.W. and G.K. Torrington, "Infrared Viewer for Turbine Engine Internal Surfaces, Phase I Final Report," QUEST Technical Report No. 623, Quest Integrated, Inc., Kent WA, June, 1994.

6. www.aeromet.com, Aeromet, Inc., Tulsa, OK

7. Jalbert, P.A., V.A. Zaccardi, and K.P. Baker, "Recent Improvements in the Near-Real Time Emission Measurement and Analysis Capability at AEDC", *Aerospace Engineering*, Vol. 16, No. 9, pages 25 - 31,SAE International, Brimfield, OH, September, 1996 .

8. Howard , R.P., et al, "Experimental Characterization of Gas Turbine Emissions at Simulated Flight Altitude Conditions," AEDC-TR-96-3, September, 1996.

9. "Procedure for the Calculation of Gaseous Emissions from Aircraft Turbine Engines." SAE ARP1533, April 30, 1982.

10. "TEP™ for Windows, A Combustion Analysis Tool," Version 1.0 Users Manual, Software Engineering Associates, Inc. 333 S. Carson Meadow, Suite 44, Carson City, NV, 89701.

11. Incropera, F.P., and D.P. DeWitt, Fundamentals of Heat and Mass Transfer, , Third Edition, John Wiley and Sons, New York, NY, 1990.

12. Kreith, Frank, Principles of Heat Transfer, International Textbook Company, Scranton, PA, 1958.

13. Walker, J. et al, "Handbook of the Standardized Infrared Radiation Model (SIRRM)." AFRPL-TR-81-61, 1981.

14. Microsoft Excel ™ is a registered trademark of the Microsoft Corporation.

15. Dougherty, R. L., and J. B. Franzini, "Fluid Mechanics with Engineering Applications," Sixth Edition, McGraw-Hill, Inc., New York, NY, 1965.

16. Personal communication with Ms. Celia A. Doub, Sverdrup Technology, Inc. AEDC Group.

17. Power, G.D., G.K. Cooper, and J.R. Sirbaugh, "NPARC 2.2 - Features and Capabilities," AIAA 95-2609, July, 1995.

18. Personal communication with Mr. Michael A. McClure, Sverdrup Technology, Inc. AEDC Group.

19. Collins, F., "Description of the University of Tennessee Space Institute Water Tunnel," UTSI 82-1, January 1982.

20. McDaniel, D.M., "Background and Theoretical Considerations for Utilizing Water Tunnel Flow Visualization," M.S. Thesis, University of Tennessee, August 1986.

APPENDIX A

Tables and Figures

Table 1. Combustor Exhaust Gas Properties

	TYPICAL DATA	TEP™ PREDICTIONS	% DIFF.
Reactants			
Fuel - Natural Gas	$C_{1.031}H_{4.17}$	$C_{1.031}H_{4.17}$	
Oxidizer - Air (98.72 %)	$N_{1.562}O_{.4196}AR_{.009}C_{.0003}$	$N_{1.562}O_{.4196}AR_{.009}C_{.0003}$	
Oxidizer - Water (1.28 %)	H_2O	H_2O	
Gas Composition			
N_2, %	74.29	73.18	-1.5
O_2, %	11.78	11.4	-3.3
H_2O, %	9.95	10.05	1.0
CO_2, %	3.95	4.04	2.2
HC, ppm	7.8	N/A	N/A
NO_x, ppm	60.1	3927	98.5
CO, ppm	95.2	13	-632.3
NO, ppm	41.9	3906	98.9
NO_2, ppm	18.2	21	13.3
Gas Properties			
MW, $^{lbm}/_{lbmole}$	28.123	28.216	0.33
C_P, $^{BTU}/_{lbm\text{-}R}$	0.25	0.3376	25.95
RGC, $^{ft\text{-}lbf}/_{lbm\text{-}R}$	54.938	54.767	-0.31
GAMMA	1.394	1.277	-9.16
Static Pressure, psia	184.4	184.4	
Pitot Pressure, psia	189.9	189.9	
Flame Temp., R	3359	3359	
Total Temp., R	3386	3386	
Mach Number	0.201	0.212	5.01
Velocity, $^{ft}/_{sec}$	578.9	578.9	
Density, $^{lbm}/_{ft3}$	0.144	0.144	0.07
Absolute Viscosity, $^{lbf\text{-}s}/_{ft2}$		1.28E-6	
Therm. Conductivity, $^{lbf}/_{s\text{-}R}$		0.0145	
Reynolds Number (d = 0.0783 ft)		158,494	
Prandtl Number		0.7131	

Successful Pitot / Emission Probe Design

Advantages

Single access through duct wall required.
Single probe provides two measurements.
Averaged measurements across duct.
Water cooling maintains structural integrity.
High probe temperature keeps gas sample vaporized.

Disadvantages

Welded internal tube fabrication.
Intrusive measurement technique.

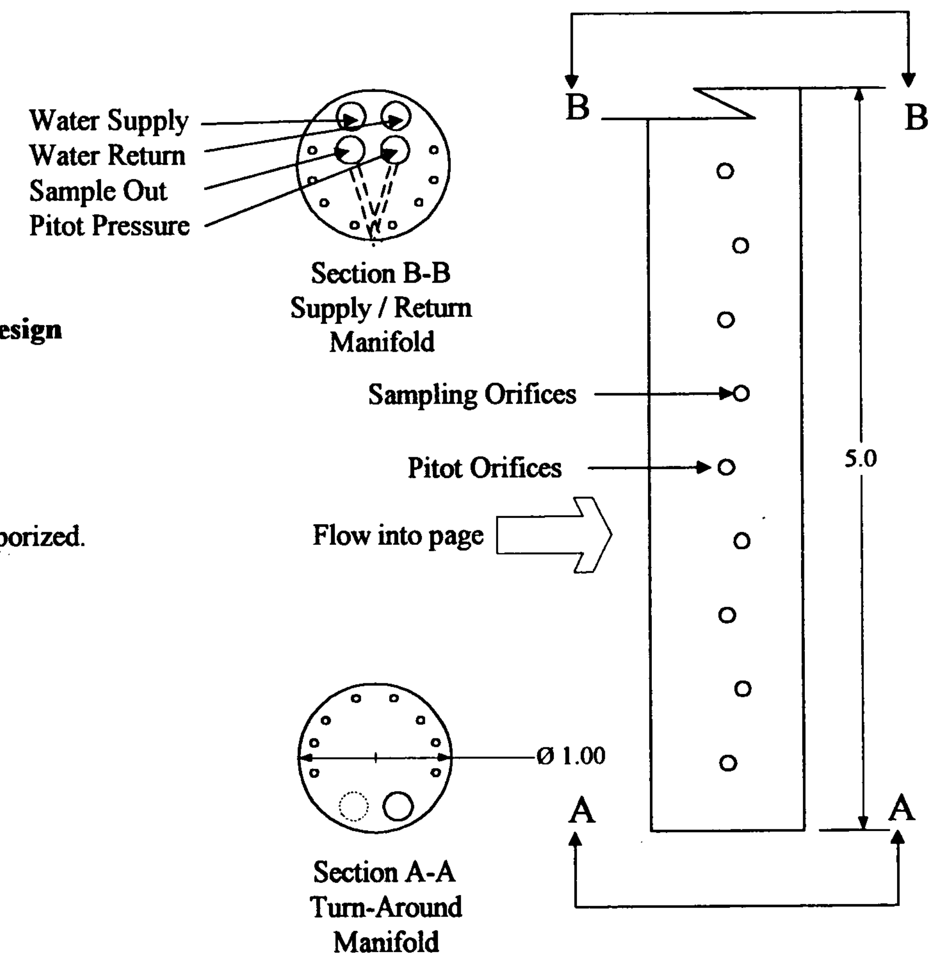

Figure 1. Water Cooled Pitot Emission Probe Assembly

Baseline Optical Survey Concept

Advantages

Nonintrusive measurement.
Easy fabrication.
Long optical path length.
Easy access to optical components.
Water cooling modeled after successful designs.
Rearward - facing step and purge help clear optical surfaces.

Disadvantages

Must maintain optical alignment of two probes.
Measurement crosses entire flow.
Dual access through duct wall required.

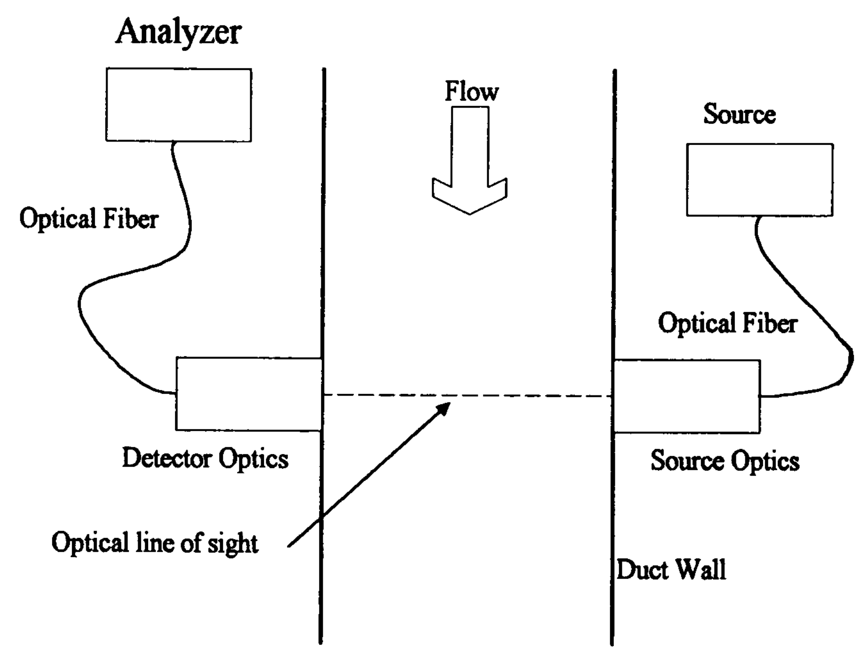

a. Baseline Optical Survey Concept
Figure 2. Hybrid Probe Concepts

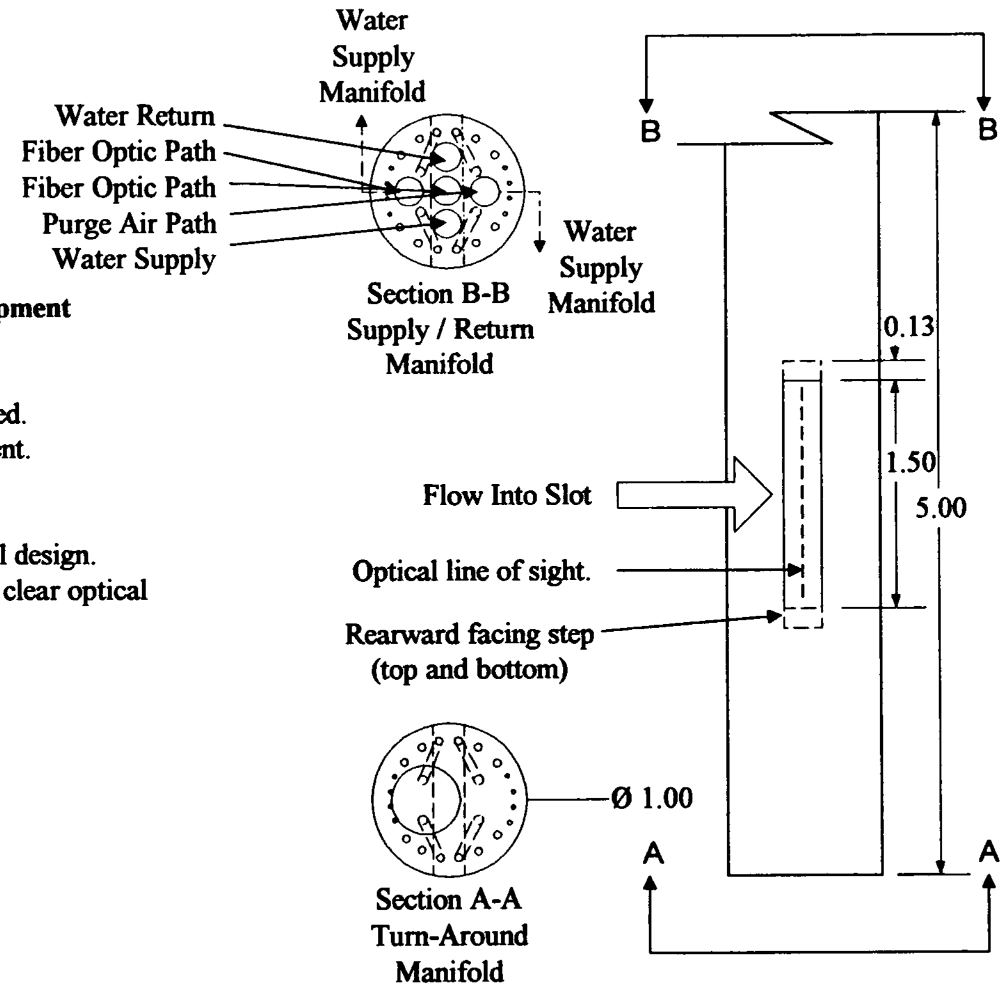

Concept Selected for Development

Advantages
Minimally intrusive measurement
Single access through duct wall required.
Single probe maintains optical alignment.
Measurement at flow centerline.
Easy access to optical components.
Water cooling modeled after successful design.
Rearward - facing step and purge help clear optical surfaces.

Disadvantages
Short optical path length.
Complex fabrication.

b. Concept Selected for Development
Figure 2. (Continued)

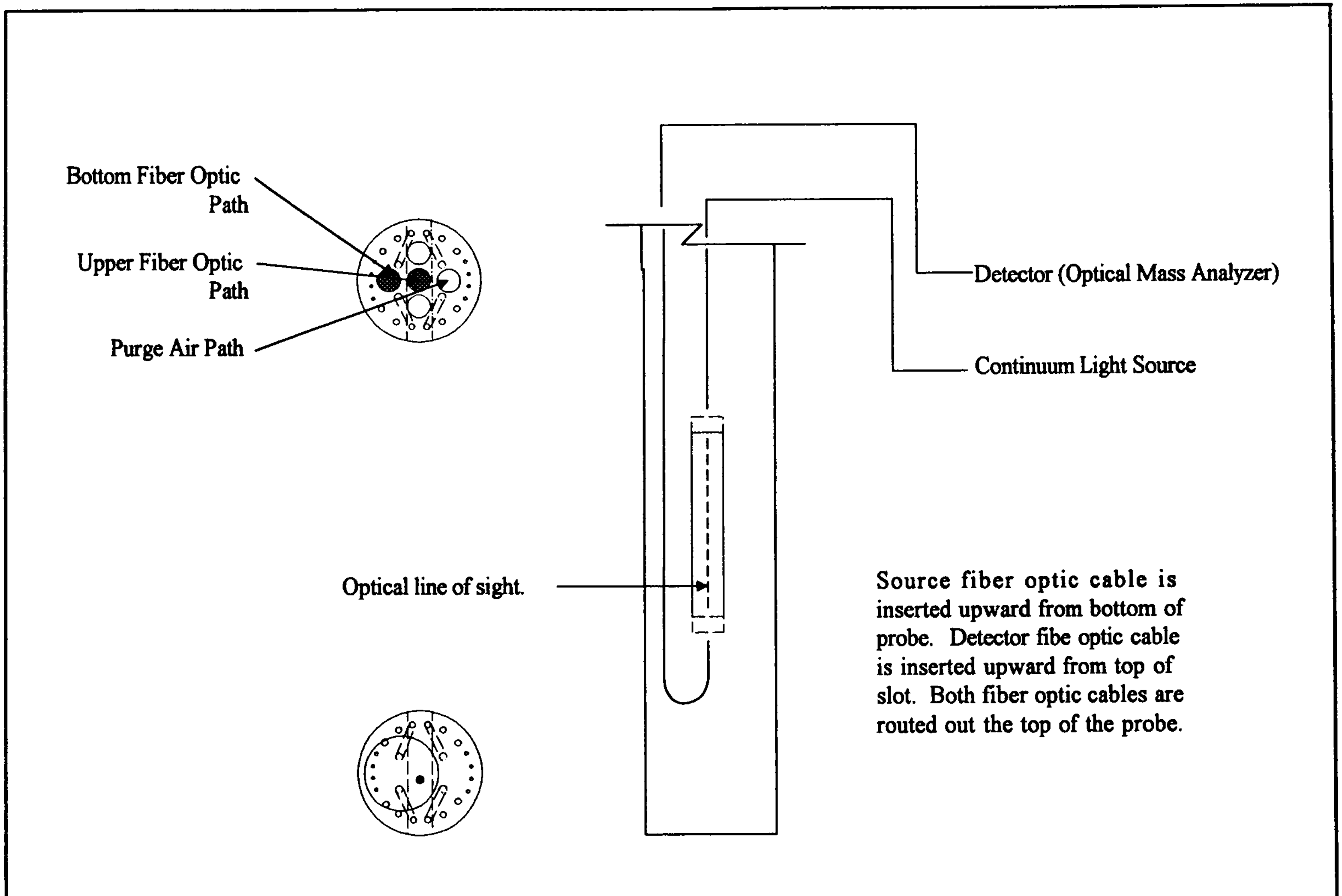

c. Optical Components
Figure 2. (Concluded)

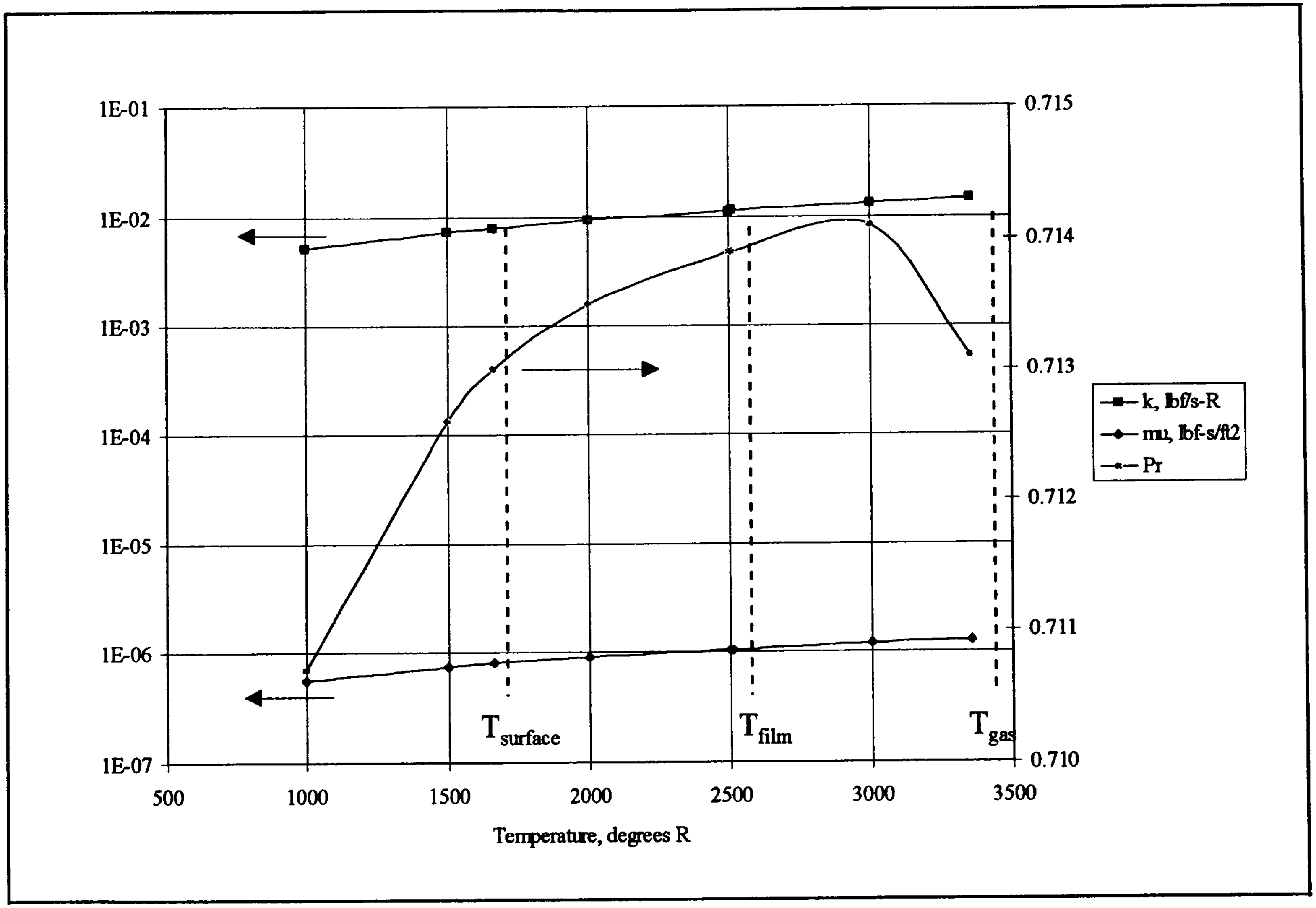

Figure 3. Gas Properties versus Temperature

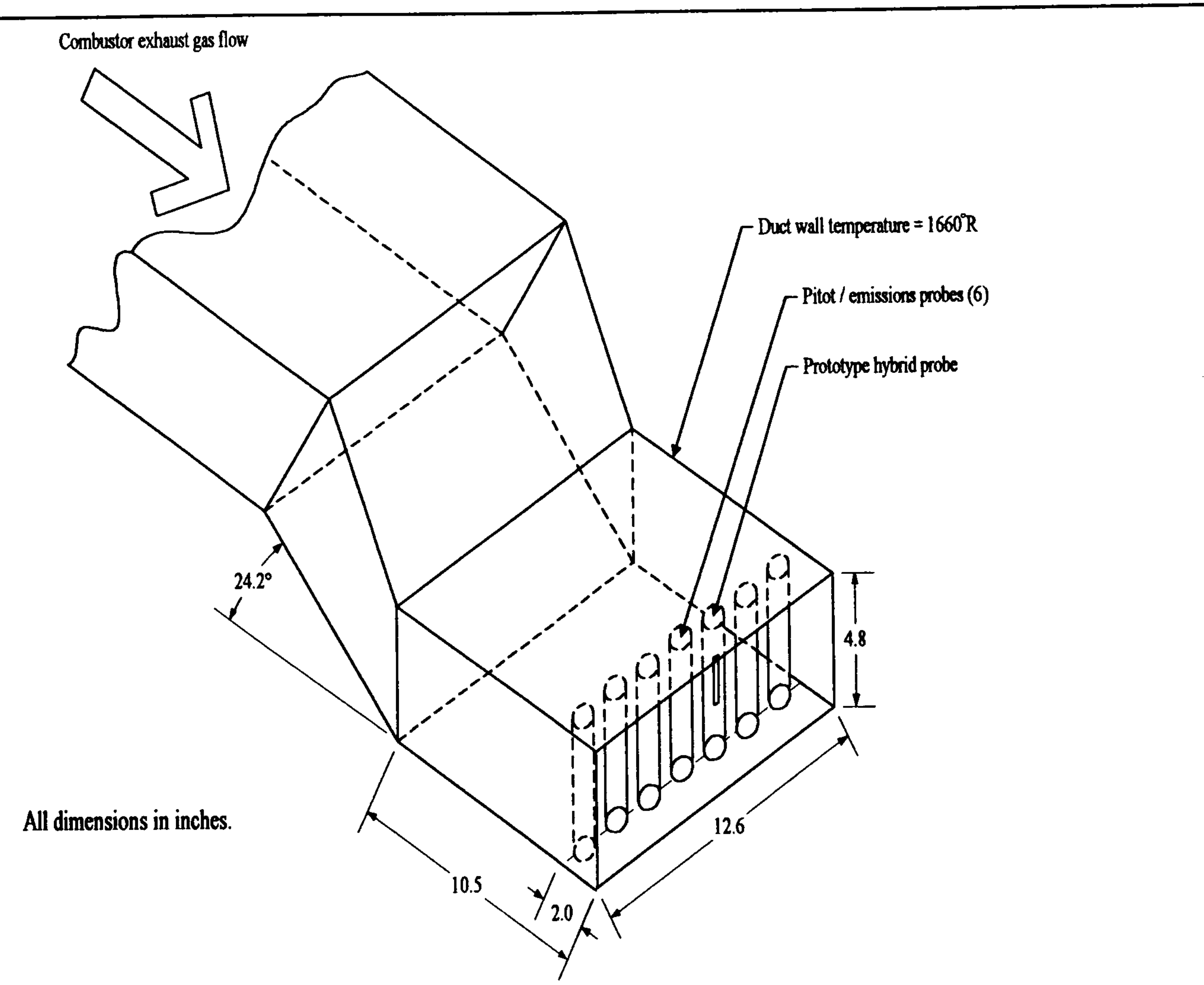

Figure 4. Combustor Duct Geometry

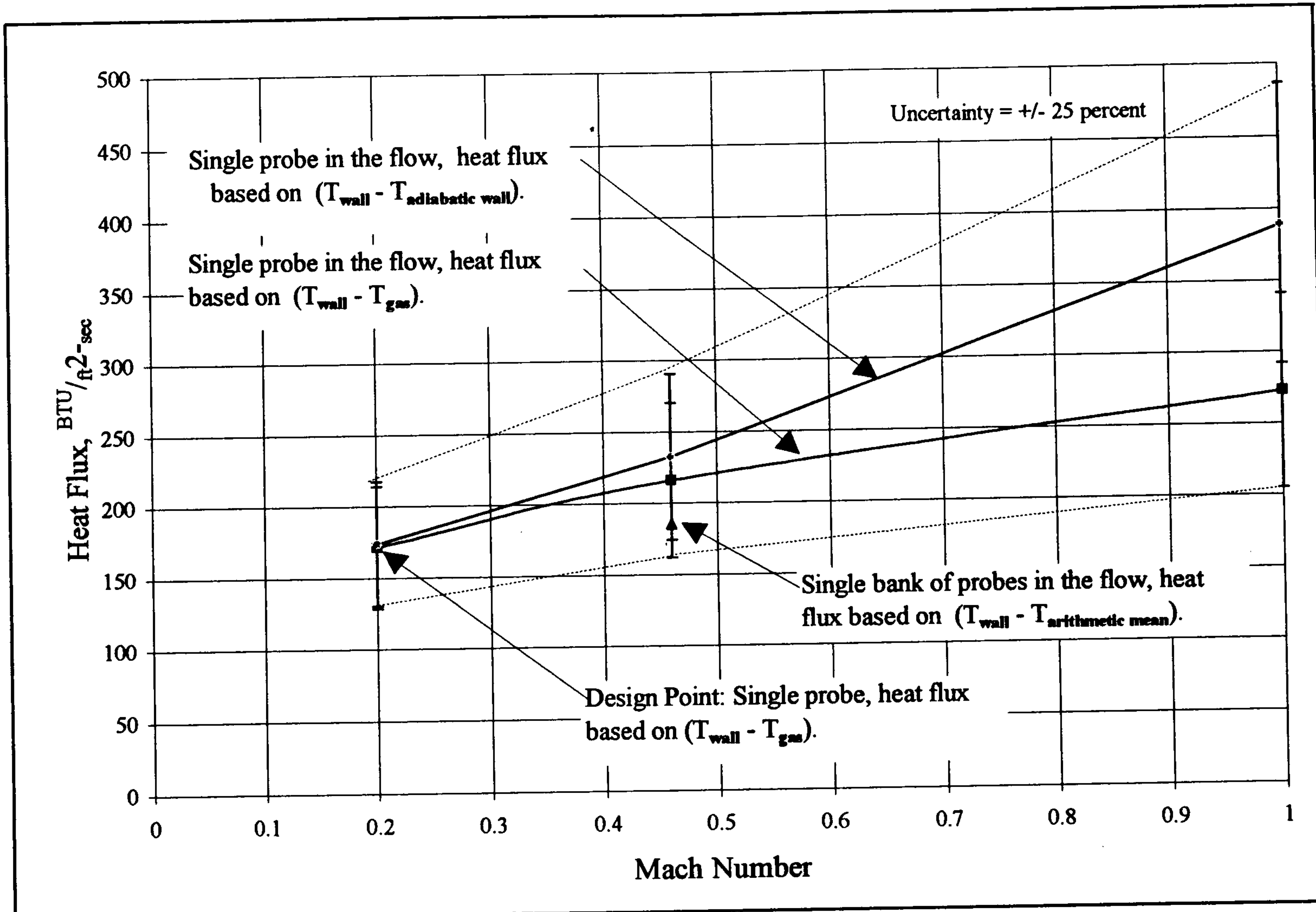

Figure 5. Convective Heating Model Options

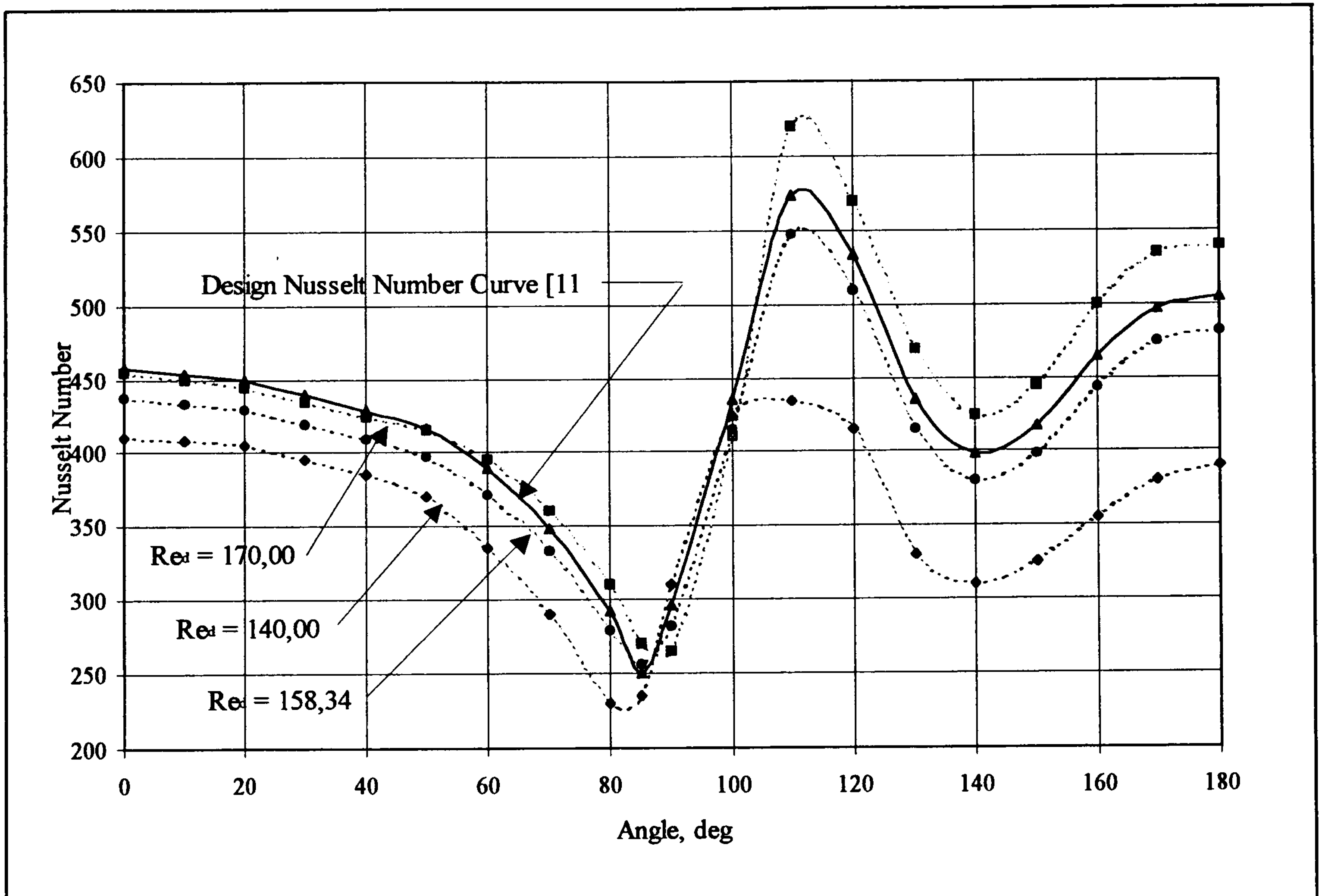

Figure 6. Nusselt Number Distribution Over Probe Surface

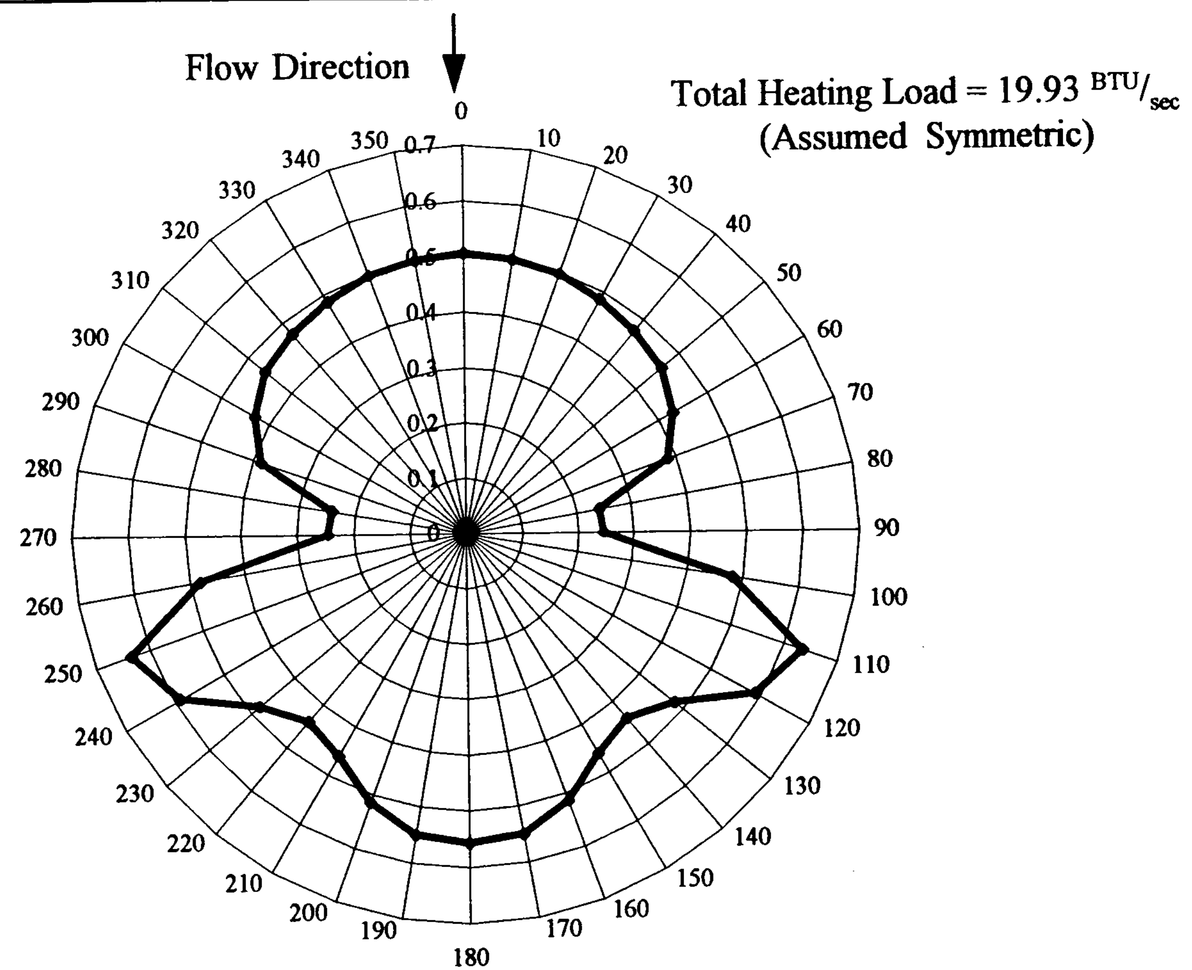

Figure 7. Total Heating Load Distribution Over Probe

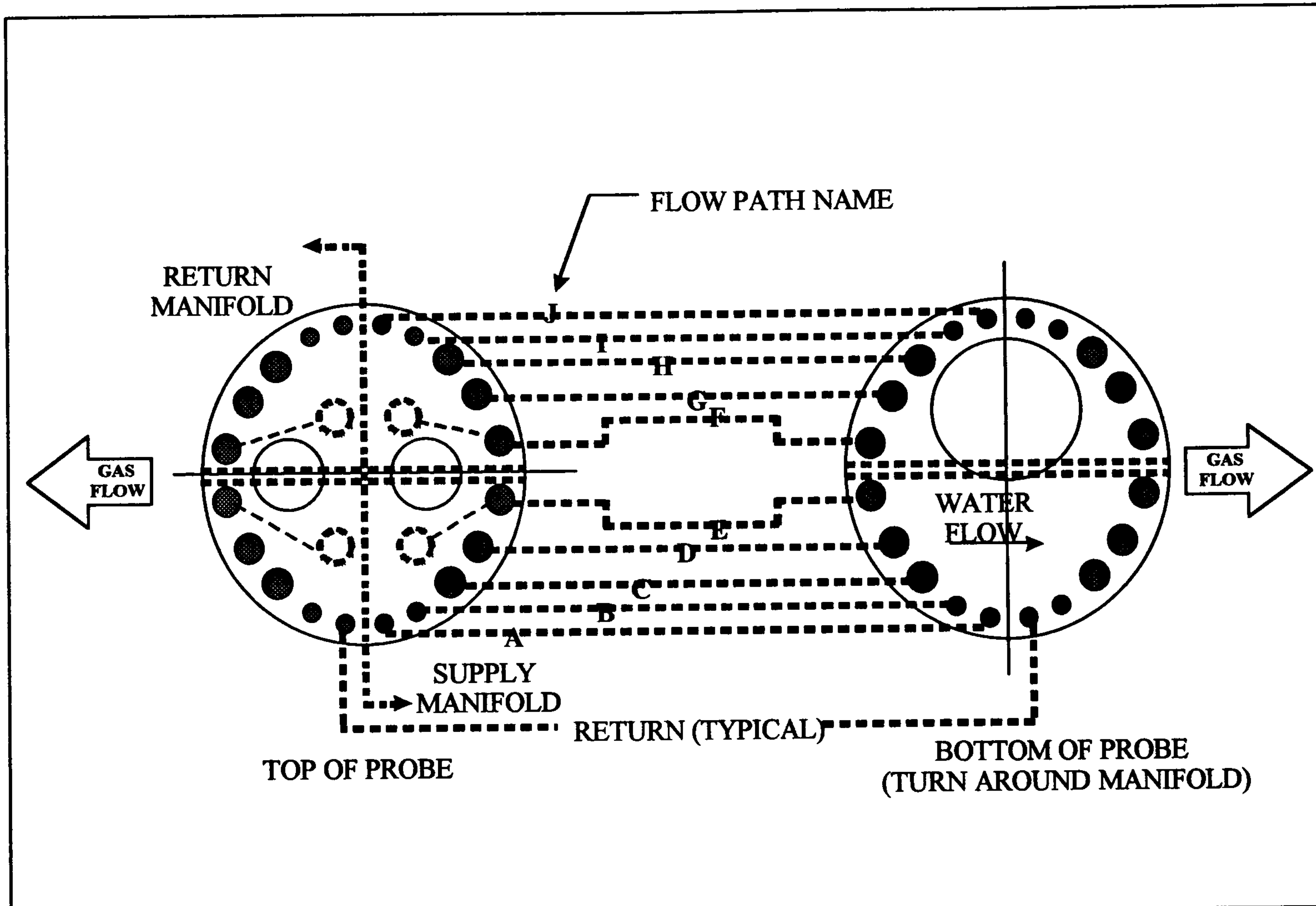

Figure 8. Probe Hydraulic Schematic

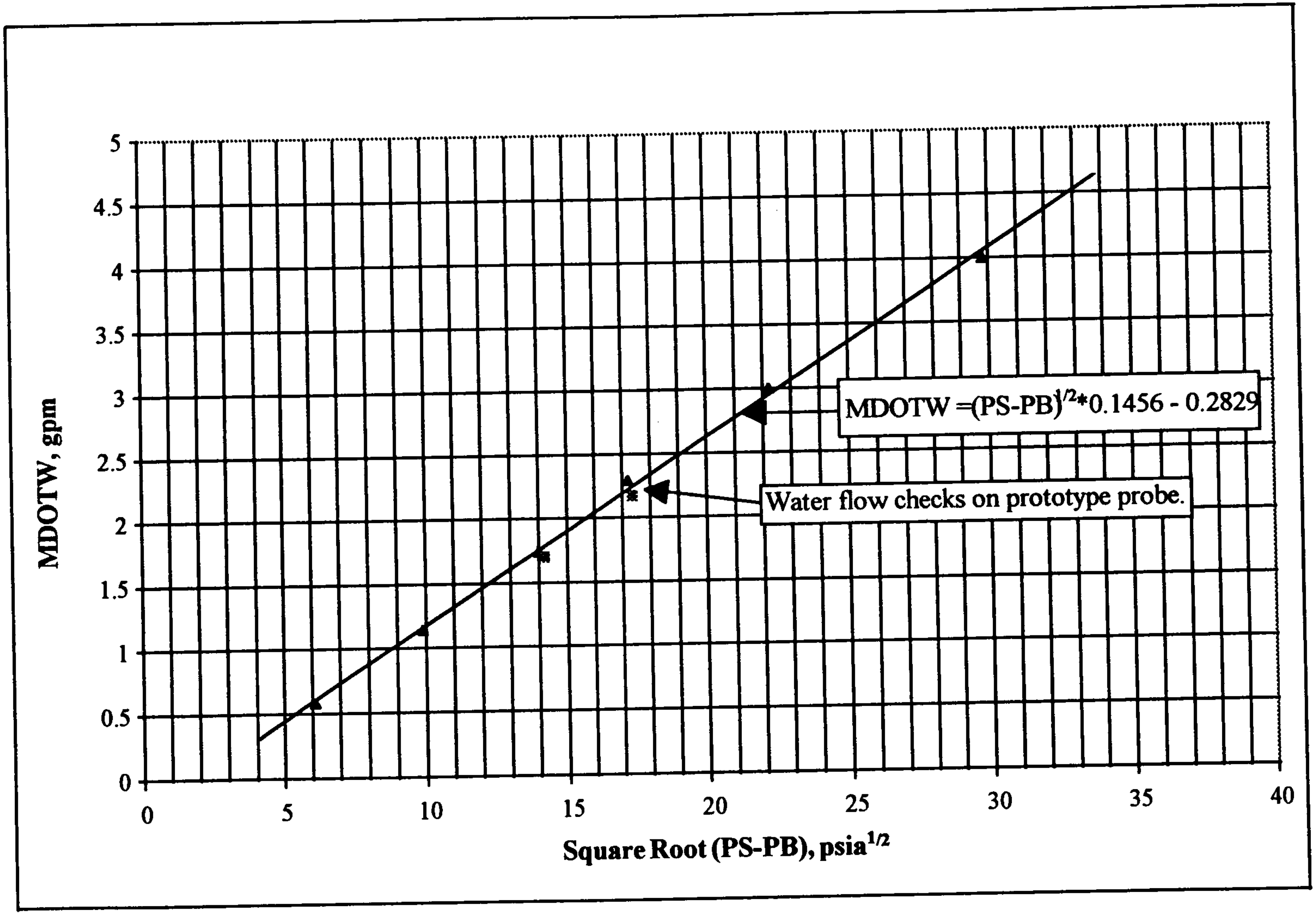

Figure 9. Water Flow Rate versus Supply Pressure

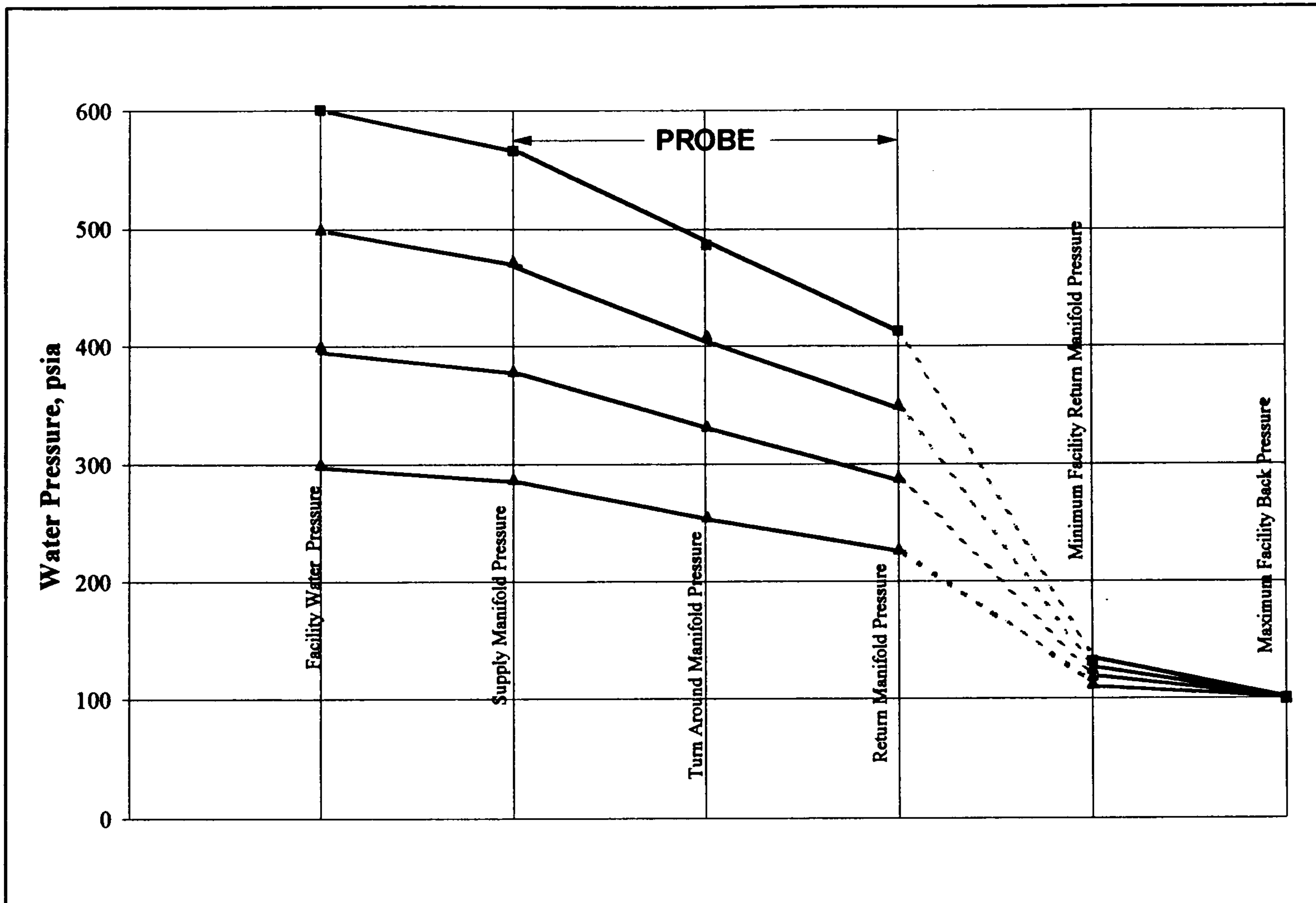

Figure 10. Water Pressure Loss Through the Probe

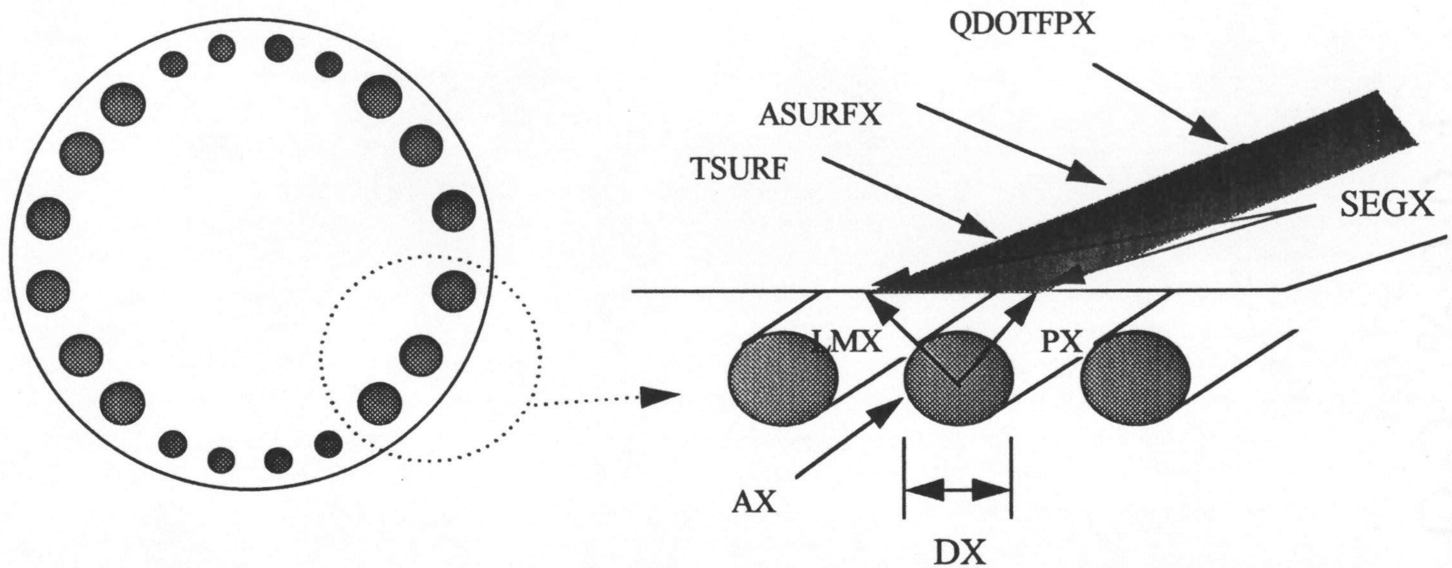

NOMENCLATURE
SEGX = angular portion of probe surface cooled by a given cooling water passage.
ASURFX= probe surface area contained within SEGX along length of probe.
DX = diameter of cooling water passage.
AX = cross sectional area of cooling water passage.
PX = perimeter of cooling water passage over length of probe.
LMX = thermal path length from cooling water passage to surface segment.
QDOTFPX = total heat load to surface area segment above each flow path.

Figure 11. One-Dimensional Heat Flux Model of the Probe Surface

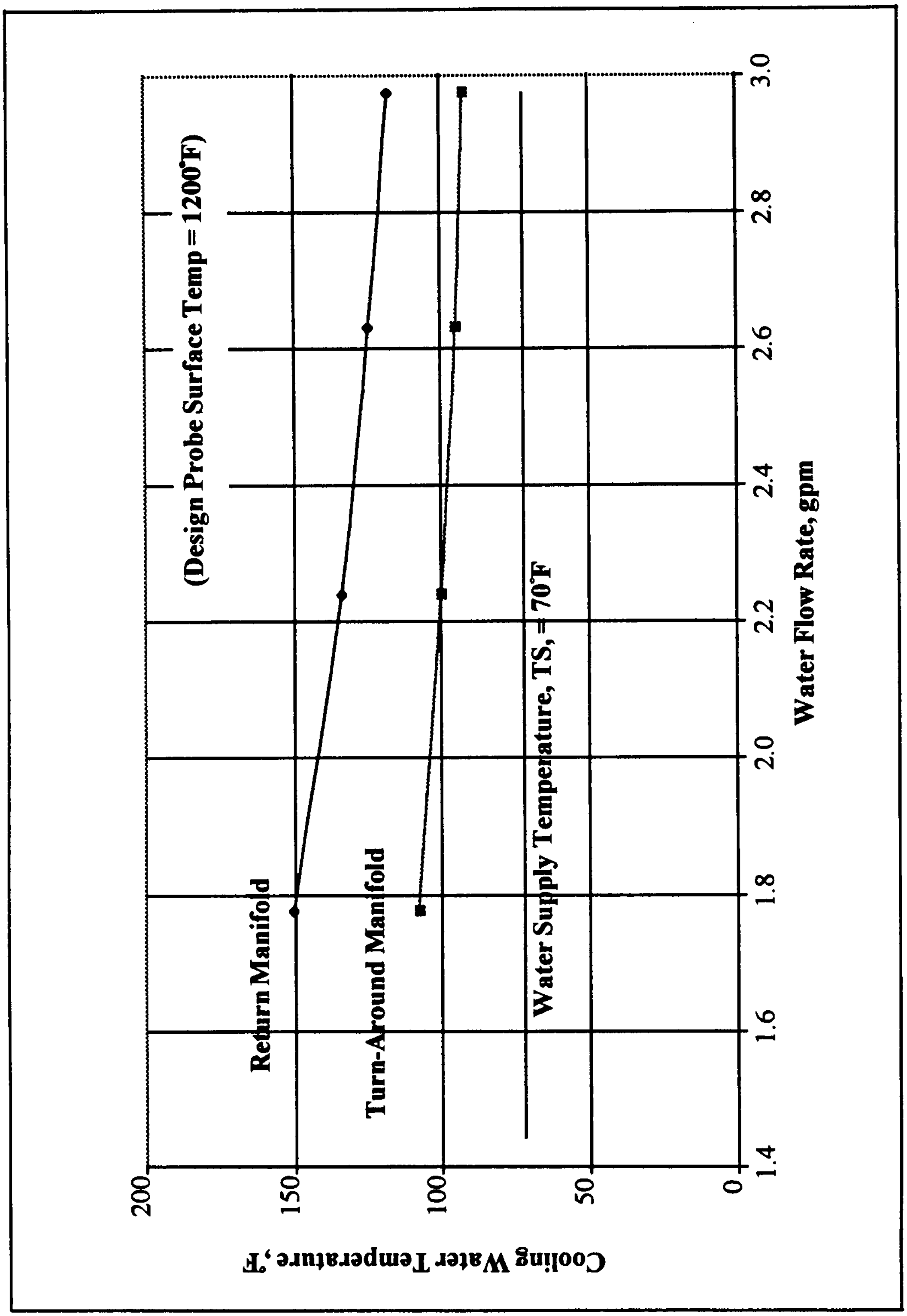

Figure 12. Water Temperature Increase Across the Probe

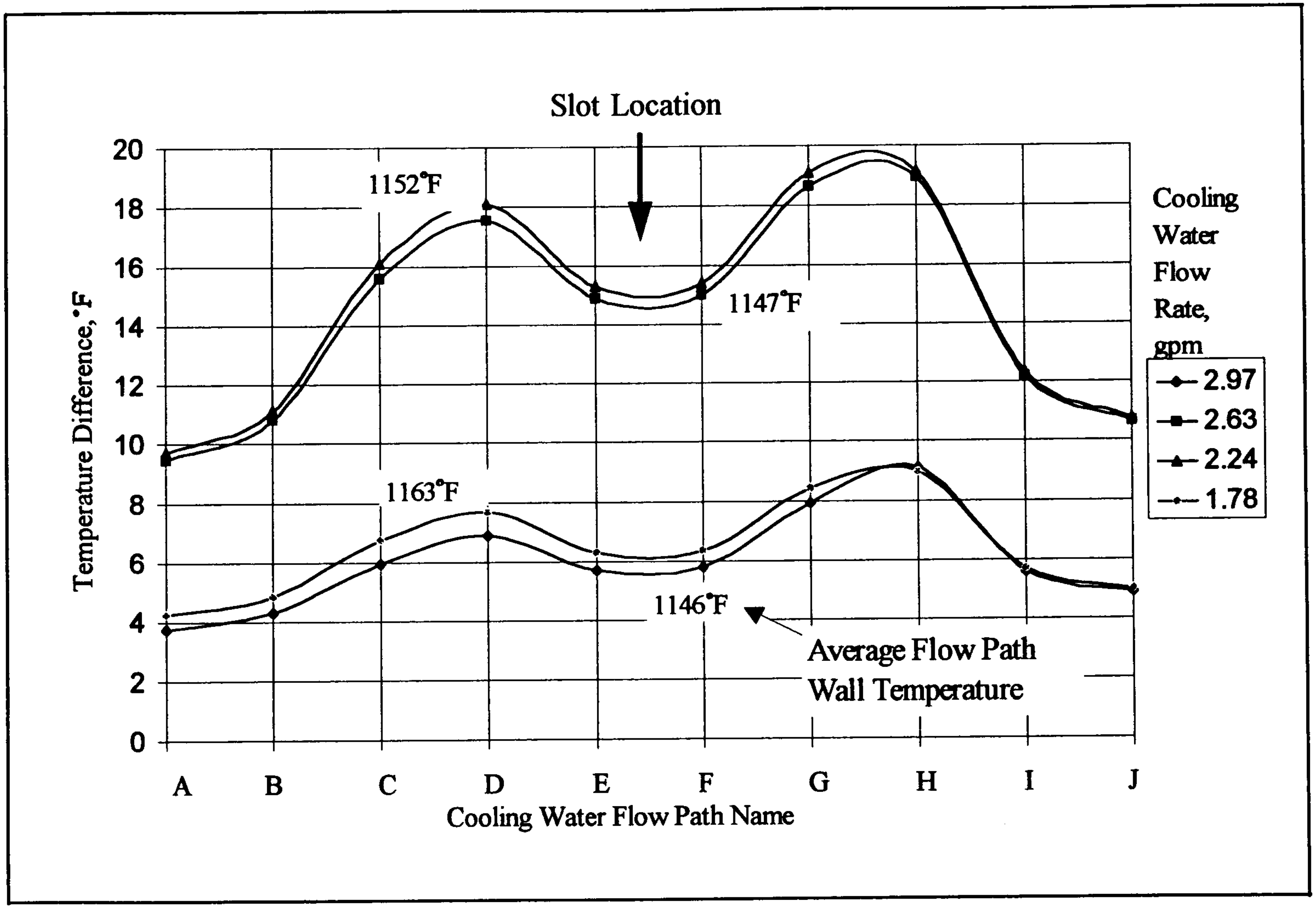

Figure 13. Effect of Thermal Deformation on Optical Alignment

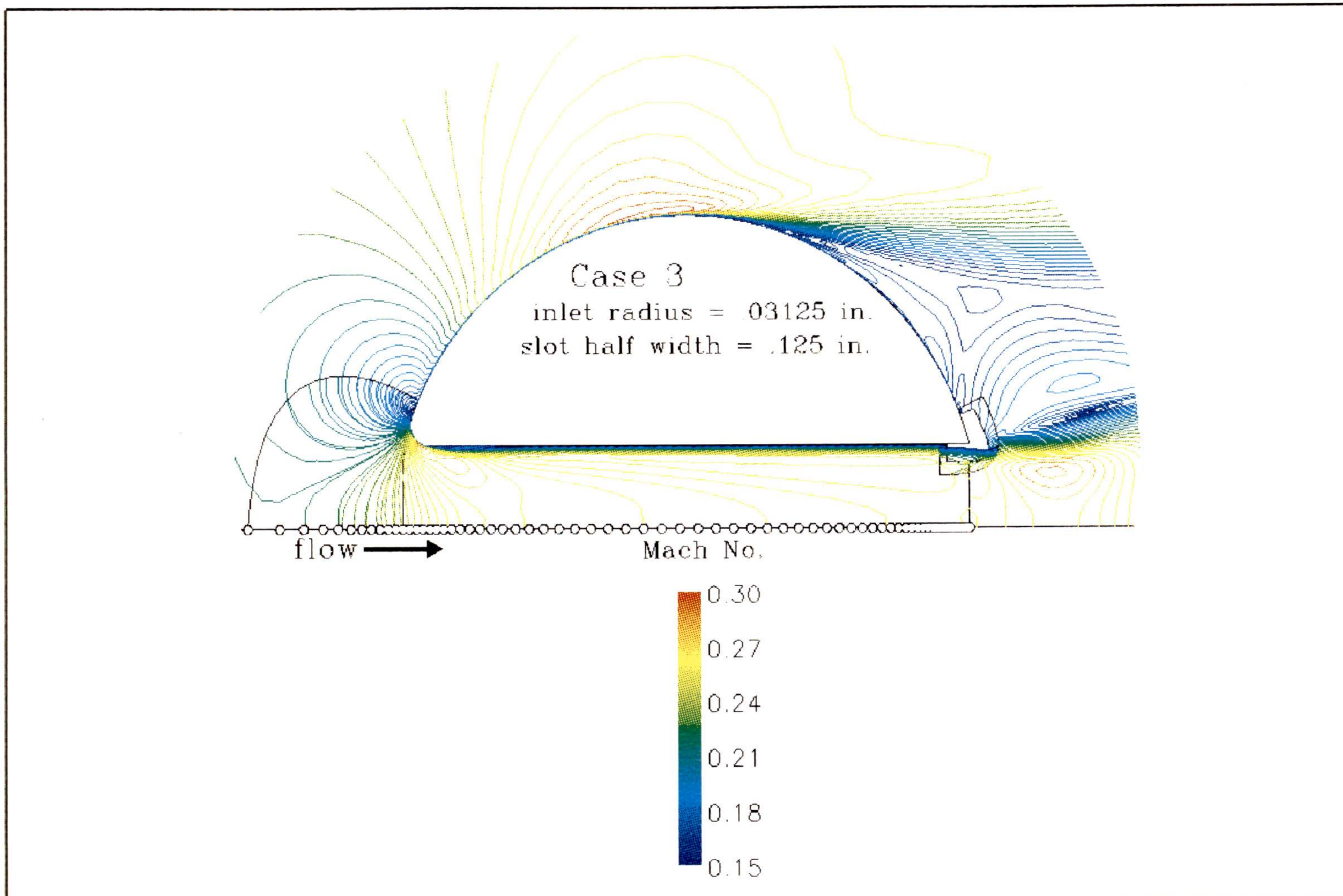

a. Variation of Mach Number Over the Probe Cross Section
Figure 14. NPARC Solution (provided by Michael A. McClure, Sverdrup Technology, Inc.)

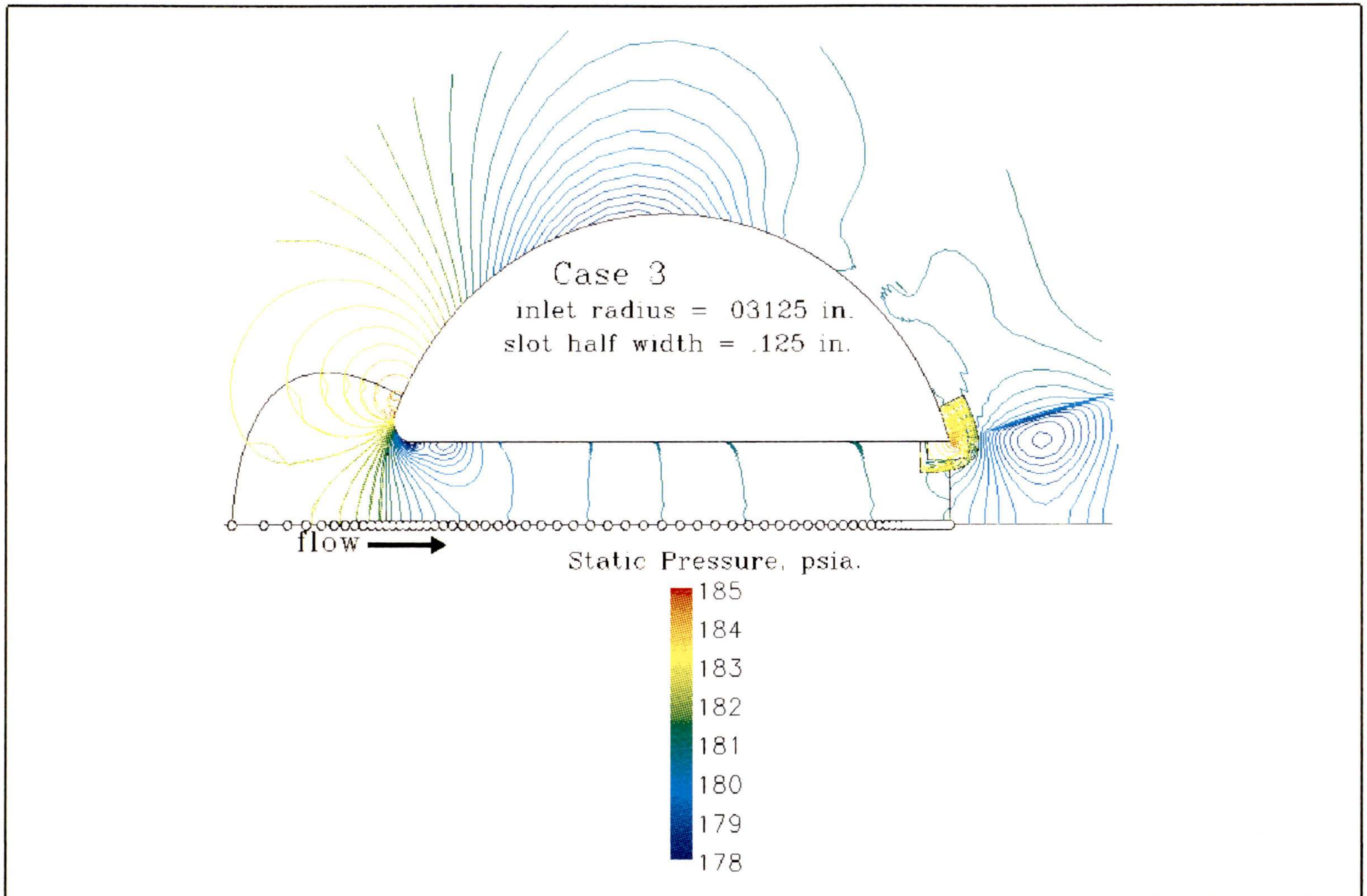

b. Variation of Static Pressure Over the Probe Cross Section
Figure 14. (Continued)

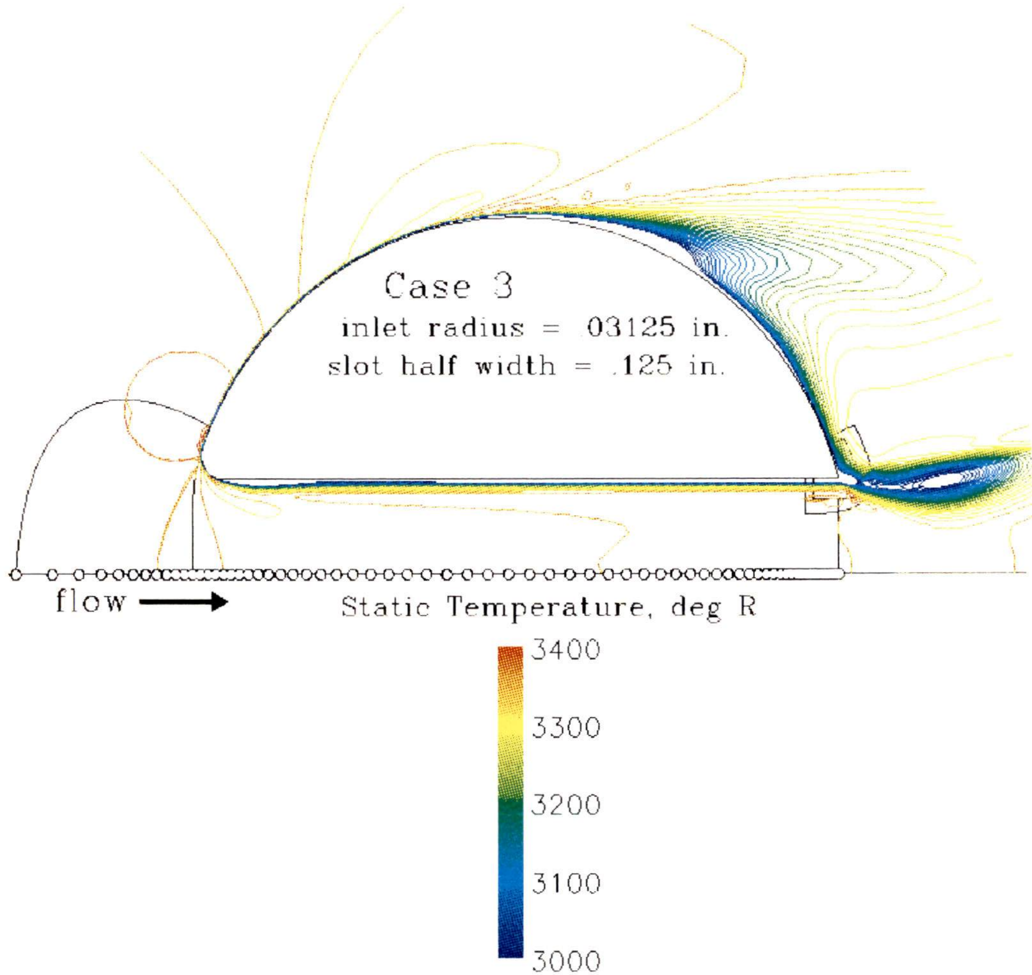

c. Variation of Static Temperature Over the Probe Cross Section
Figure 14. (Continued)

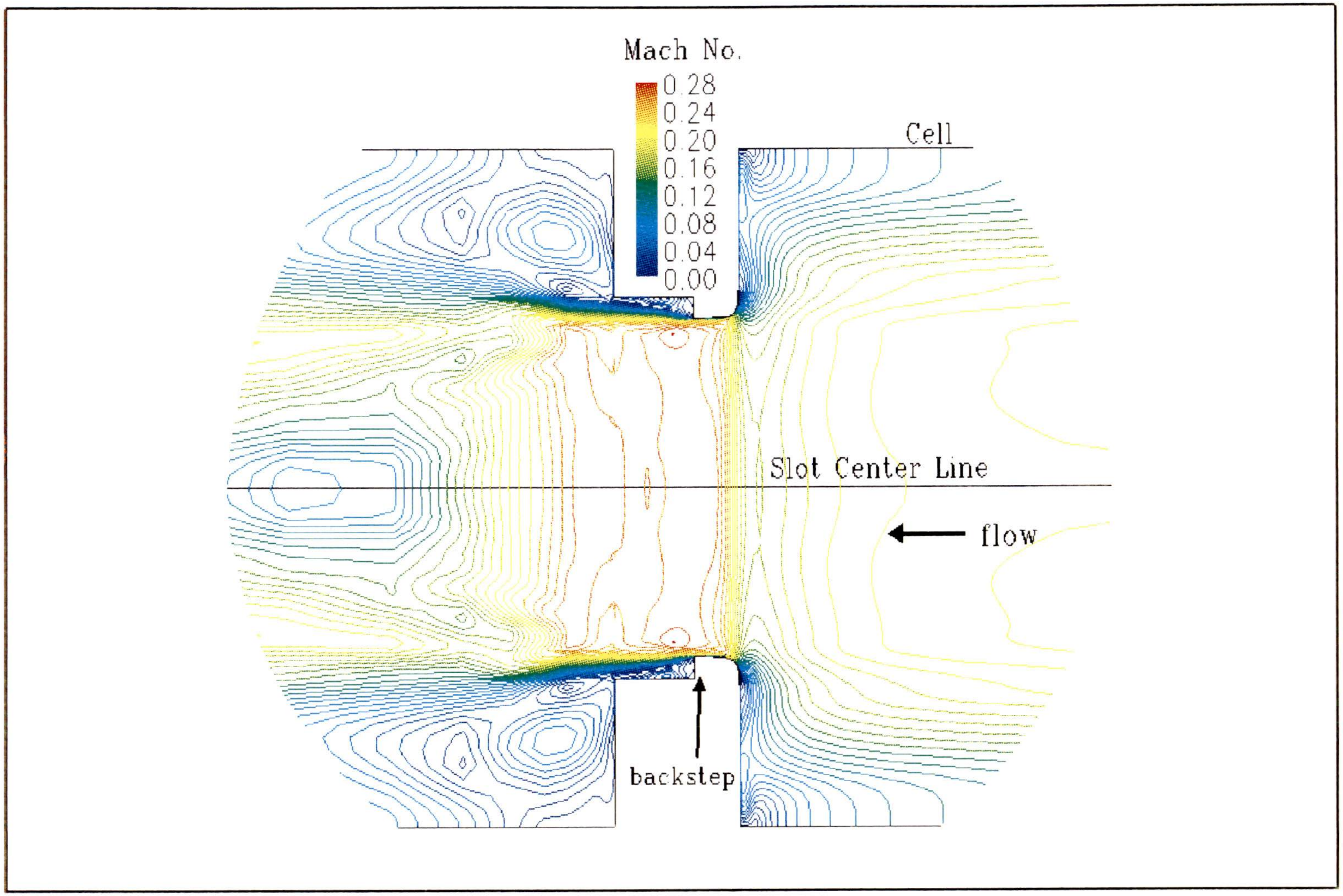

d. Vertical Variation of Mach Number in the Slot and Effect of Rearward Facing Step.
Figure 14. (Concluded)

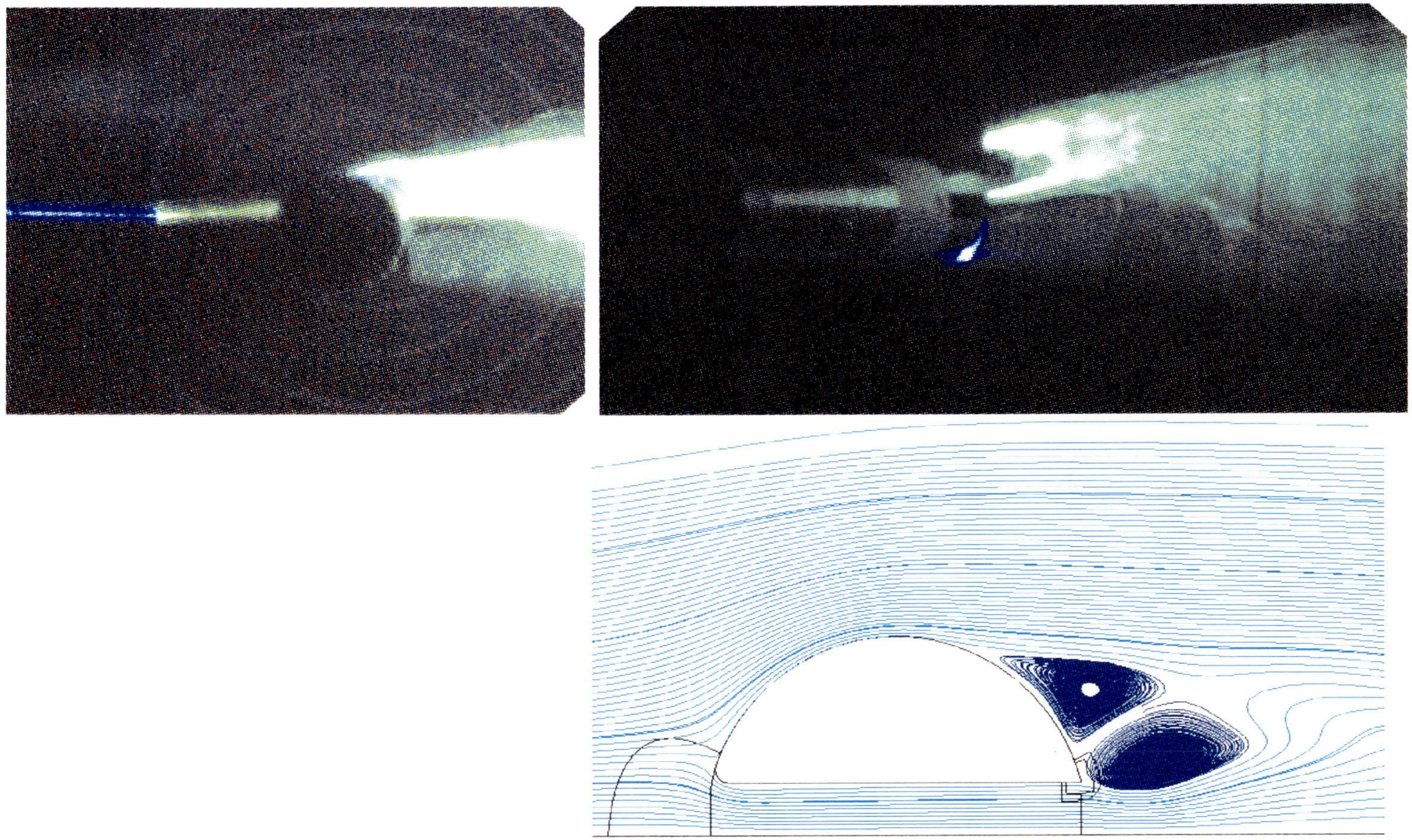

Figure 15. UTSI Water Tunnel Test Results. Top left view: dye injected at the stagnation point illuminating flow inside the slot and over the probe exterior. Top right view: dye injected through the slot illuminating flow exiting from the slot. Bottom right view: NPARC three-dimensional solution showing streamline flow.

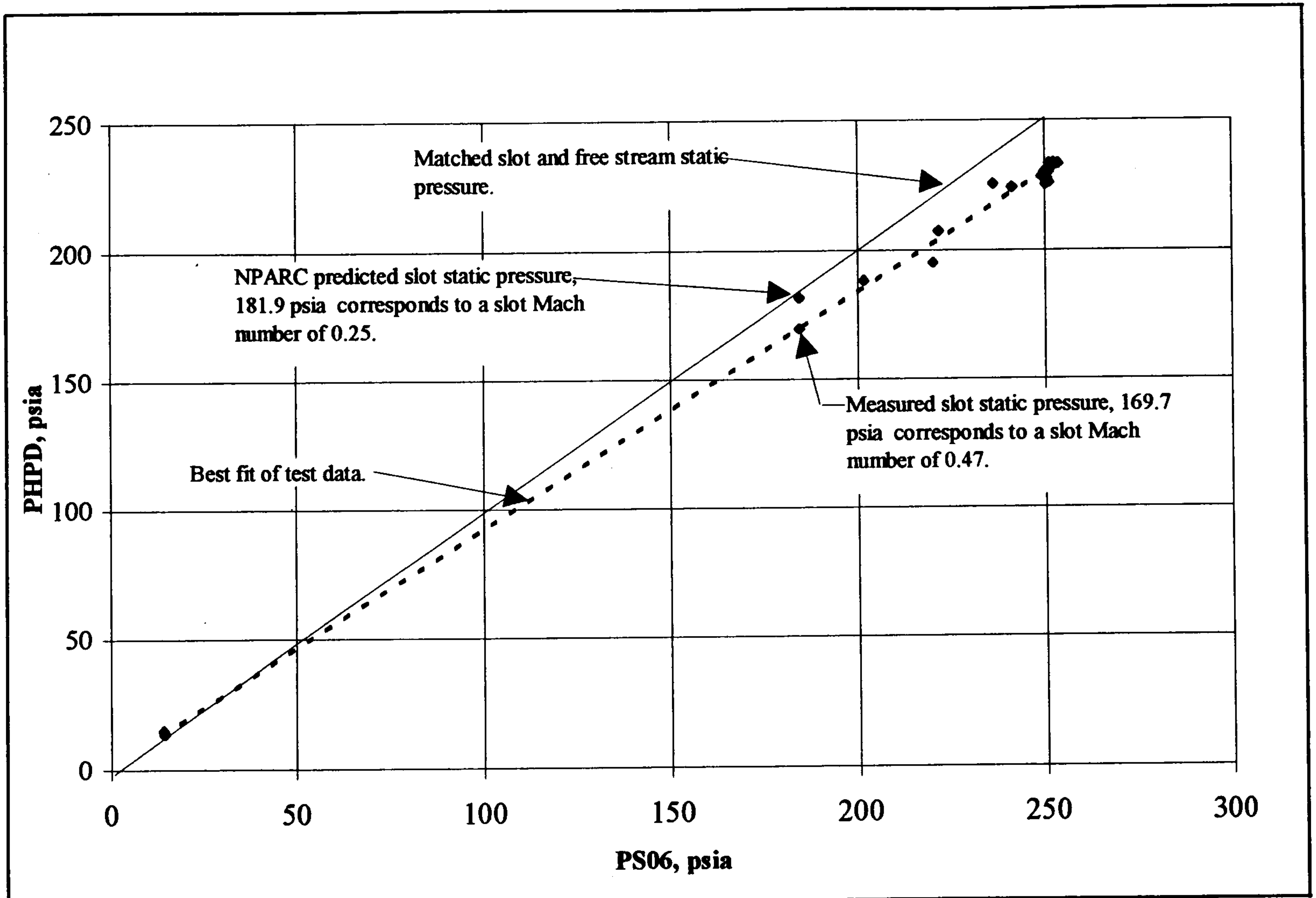

Figure 16. Slot Static Pressure versus Free Stream Static Pressure

APPENDIX B

Summary of Gas Property Calculations

Background

The method of calculations contained in this Appendix were used to specify the gas properties at the hybrid probe design conditions. The basic combustion equation for hydrocarbon fuel and air is:

$$C_M H_N + X\left[R[O2] + S[N2] + T[CO2] + SPHUM1[H2O]\right] =$$
$$P1[CO2] + P2[N2] + P3[O2] + P4[H2O] + P5[CO] + P6[C_X H_Y] + P7[NO2] + P8[NO]$$

where P1, P2, P3, P4, P5, P6, P7, and P8 are the number of moles of each species produced in the combustion of one mole on fuel, C_MH_N , with X moles of air. The form of the unburned fuel, C_XH_Y, is assumed to be the same as C_MH_N. A matrix solution of ten simultaneous equations is used to solve for the P terms.

C Balance: M + T*X = P1 + P5 + M*P6

H Balance: N + 2*SPHUM1*X = 2*P4 + N*P6

O Balance: (2*R + 2*T + SPHUM1)*X = 2*P1 + 2*P3 + P4 + P5 + 2*P7 + P8

N Balance: 2*S*X = 2*P2 + P7 + P8

P1 = PT*[CO2] (where [CO2] is the measured CO_2 concentration)

P5 = PT*[CO] (where [CO] is the measured CO concentration)

M*P6 = PT* [C_MH_N] (where [C_MH_N] is the measured C_MH_N concentration)

P7 + P8 = PT*[NOX] (where [NOX] is the measured NO_X concentration)

P8 = PT * [NO] (where [NO] is the measured NO concentration)

PT = P1 + P2 + P3 + P4 + P5 + P6 + P7 + P8 (where PT is the total number of moles)

Constants And Seldom Changed Variables

NAME	VALUE	DESCRIPTION
MWAIR	28.965	molecular weight of air
MWC	12.011	atomic weight of carbon
MWCO	28.0104	molecular weight of carbon monoxide
MWCO2	44.0098	molecular weight of carbon dioxide
MWH	1.008	atomic weight of hydrogen
MWN	14.0067	atomic weight of nitrogen
MWNO	30.0061	molecular weight of nitric oxide
MWNOX	46.0055	molecular weight of nitrous oxide
MWNO2	46.0055	molecular weight of nitrogen dioxide
MWO	15.9994	atomic weight of oxygen
MWNG	16.586	molecular weight of natural gas
MWCH4	16.043	molecular weight of methane
MWH20	18.0154	molecular weight of water
R	0.20948	mass fraction of O_2 in air
S	0.7902	mass fraction of N_2 and Ar in air
T	0.00032	mass fraction of CO_2 in air
L	0	CO_2 interference on CO
M	0	H_2O interference on CO
LPRIME	0	CO_2 interference on NOx
MPRIME	0	H_2O interference on NOx

J	0	O_2 interference on CO_2
ETA	0.975	NOx converter efficiency
M1	12.2801	Enthalpy curve fit, CO2 slope
B1	-1822.48	Enthalpy curve fit, CO2 intercept
M2	7.60735	Enthalpy curve fit, N2 slope
B2	-311.267	Enthalpy curve fit, N2 intercept
M3	8.06743	Enthalpy curve fit, O2 slope
B3	-480.476	Enthalpy curve fit, O2 intercept
M4	9.48444	Enthalpy curve fit, H2O slope
B4	-694.484	Enthalpy curve fit, H2O intercept
M5	7.69892	Enthalpy curve fit, CO slope
B5	-347.429	Enthalpy curve fit, CO intercept
M6	15.4444	Enthalpy curve fit, CH4 slope
B6	-3200.39	Enthalpy curve fit, CH4 intercept
M8	7.88043	Enthalpy curve fit, NO slope
B8	-281.971	Enthalpy curve fit, NO intercept
HFCO2	-93,987.5	CO2 Enthalpy of formation, cal/mole
DHCO2	2,238.11	CO2 Absolute enthalpy at 298 K, cal/mole
HFCO	-26,392.9	CO Enthalpy of formation, cal/mole
DHCO	2,072.63	CO Absolute enthalpy at 298 K, cal/mole
HFNO	21,544.3	NO Enthalpy of formation, cal/mole
DHNO	2,194.2	NO Absolute enthalpy at 298 K, cal/mole

HFH2O	-57,753.9	H2O Enthalpy of formation, cal/mole
DHH2O	2,367.7	H2O Absolute enthalpy at 298 K, cal/mole
HFCH4	-17,770.4	CH4 Enthalpy of formation, cal/mole
DHCH4	2,397.0	CH4 absolute enthalpy at 298 K, cal/mole
DHN2	2,072.3	N2 Absolute enthalpy at 298 K, cal/mole
DHO2	2,069.8	O2 Absolute enthalpy at 298 K, cal/mole
GC	32.174	Gravitational constant, ft-lbm/lbf-sec^2

Required Measurements

[CO]	measured semi-dry carbon monoxide concentration, ppm
[CO2]	measured semi-dry carbon dioxide concentration, percent
[O2]	measured semi-dry oxygen concentration, percent
[HC]	measured wet unburned hydrocarbon concentration, ppm
[NO]	measured semi-dry nitric oxide concentration, ppm
[NO_x]	measured semi-dry nitrous oxide concentration, ppm
PSO6	measured inlet air static (and total) pressure, psia
TGO6	inlet air total temperature, °F
PS12	combustor exit static pressure, psia
PT12	combustor exit total pressure, psia
SPHUM1	specific humidity of the inlet air, $moles_{WV}/mole_{AIR}$
SPHUM2	specific humidity of the gas sample before the dryer, $moles_{WV}/mole_{AIR}$
SPHUM3	specific humidity of gas sample after the dryer, $moles_{WV}/mole_{AIR}$
WAIR	inlet air mass flow rate, lbm/sec

WNGTOT	natural gas fuel flow rate, lbm/sec
AFR	air / fuel ratio from facility air and fuel flow meters
ER	equivalence ratio from facility air and fuel flow meters

<u>Fuel and Oxidizer Descriptions</u>

1. Natural gas flow rate, moles/sec

$$WNGM = \frac{WNGTOT}{MWNG}$$

2. Air flow rate, moles/sec

$$WAIRM = \frac{WAIR}{MWAIR}$$

3. Total fuel flow rate measure by the facility fuel flow meters, lbm/sec

$$WFT = WNGTOT$$

4. Total fuel flow rate, moles/sec

$$WFTM = WNGM$$

5. Number of carbon atoms in the fuel

$$EM = 1.031$$

6. Number of hydrogen atoms in the fuel

$$EN = 4.17$$

7. Lower heating value of natural gas, BTU/lbm

$$FLHV = 20{,}500$$

8. Heat of formation of natural gas, BTU/lbm

$$ENTHALPY = -17{,}770$$

Matrix "A" Construction

The elements of the ten-by-ten matrix "A" are defined as [row, column]:

[1,1]	0
[1,2]	1
[1,3]	0
[1,4]	0
[1,5]	0
[1,6]	1
[1,7]	EM
[1,8]	0
[1,9]	0
[1,10]	-T
[2,1]	0
[2,2]	0
[2,3]	0
[2,4]	0
[2,5]	2
[2,6]	0
[2,7]	EN
[2,8]	0
[2,9]	0
[2,10]	-2 * SPHUM1
[3,1]	0
[3,2]	2
[3,3]	0
[3,4]	2
[3,5]	1
[3,6]	1
[3,7]	0
[3,8]	2
[3,9]	1
[3,10]	-2 * R - SPHUM1 - 2 * T
[4,1]	0
[4,2]	0
[4,3]	2
[4,4]	0
[4,5]	0
[4,6]	0
[4,7]	0
[4,8]	1
[4,9]	1
[4,10]	-2 * S
[5,1]	(1+ SPHUM3) * [CO2]
[5,2]	-1
[5,3]	0
[5,4]	J * [CO2]
[5,5]	-1 * (1 + SPHUM3) * [CO2]
[5,6]	0
[5,7]	0
[5,8]	0
[5,9]	0
[5,10]	0
[6,1]	(1 + SPHUM3) * [CO] + SPHUM3 * M
[6,2]	L
[6,3]	0
[6,4]	0
[6,5]	- (1 + SPHUM3) * [CO] - SPHUM3 * M
[6,6]	-1
[6,7]	0
[6,8]	0
[6,9]	0
[6,10]	0
[7,1]	[HC]
[7,2]	0
[7,3]	0
[7,4]	0
[7,5]	0
[7,6]	0
[7,7]	- EM
[7,8]	0
[7,9]	0
[7,10]	0
[8,1]	(1 + SPHUM3 * (1+ MPRIME)) * [NOX]
[8,2]	LPRIME * [NOX]
[8,3]	0
[8,4]	0
[8,5]	-(1 + SPHUM3 * (1+ MPRIME)) * [NOX]
[8,6]	0
[8,7]	0
[8,8]	- ETA
[8,9]	-1
[8,10]	0
[9,1]	(1 + SPHUM3 * (1 + MPRIME)) * [NO]
[9,2]	LPRIME * [NO]
[9,3]	0
[9,4]	0
[9,5]	- (1 + SPHUM3 * (1 + MPRIME)) * [NO]
[9,6]	0
[9,7]	0
[9,8]	0
[9,9]	-1
[9,10]	0
[10,1]	-1
[10,2]	1
[10,3]	1
[10,4]	1
[10,5]	1
[10,6]	1
[10,7]	1
[10,8]	1
[10,9]	1
[10,10]	0

Matrix "B" Construction

The elements of the one-by-ten matrix [B] are defined as [row, column]:

[1,1]	EM
[2,1]	EN
[3,1]	0
[4,1]	0
[5,1]	0
[6,1]	0
[7,1]	0
[8,1]	0
[9,1]	0
[10,1]	0

Matrix Operations

Step 1: Using the EXCEL™ matrix solver, calculate the inverse of Matrix [A], $[A]^{-1}$.

Step 2: Multiply the inverse of Matrix [A] times Matrix [B] and define the solution as Matrix [C].

$$[C] = [A]^{-1} \times [B]$$

The elements of the one-by-ten Matrix [C] are defined as [row, column]:

[1,1]	PT	total number of moles
[2,1]	P1	number of moles of CO_2
[3,1]	P2	number of moles of N_2
[4,1]	P3	number of moles of O_2
[5,1]	P4	number of moles of H_2O
[6,1]	P5	number of moles of CO
[7,1]	P6	number of moles of HC
[8,1]	P7	number of moles of NO_2
[9,1]	P8	number of moles of NO
[10,1]	X	number of moles of Air

Standard Analysis Of Measured Emissions

1. Wet basis concentration of NOX, moles

$$P9 = P7 + P8$$

2. Atomic hydrogen - carbon ratio in fuel

$$ALPHA = \frac{EN}{EM}$$

3. Average exhaust gas molecular weight, lbm/mole

$$MW = \Big(P1 \times MWCO2 + P2 \times 2 \times MWN + P3 \times 2 \times MWO + P4 \times MWH2O + P5 \times MWCO + P6 \times (EM \times MWC + EN \times MWH) + P7 \times MWNO2 + P8 \times MWNO + P9 \times MWNOX \Big) \div PT$$

4. Exhaust gas constant, ft-lbf/lbm-°R

$$RGC = \frac{1545.3}{MW}$$

5. Air to fuel ratio calculated from measured emissions

$$AFREMS = \frac{X}{EM} \times \frac{MWAIR}{MWC + ALPHA \times MWH}$$

6. Air to fuel equivalence ratio calculated from measured emissions

$$AFEREMS = \frac{AFREMS}{\dfrac{2 \times MWO \times EM + 0.5 \times MWO \times EN}{MWC \times EM + MWH \times EN}}$$

Wet Basis Mole Fractions

1. $CO_2 = \frac{P1}{PT} \times 100$, percent

2. $N_2 = \frac{P2}{PT} \times 100$, percent

3. $O_2 = \frac{P3}{PT} \times 100$, percent

4. $H_2O = \frac{P4}{PT} \times 100$, percent

5. $CO = \frac{P5}{PT} \times 1{,}000{,}000$, parts per million

6. $HC = \frac{P6}{PT} \times 1{,}000{,}000$, parts per million

7. $NO_2 = \frac{P7}{PT} \times 1{,}000{,}000$, parts per million

8. $NO = \frac{P8}{PT} \times 1{,}000{,}000$, parts per million

9. $NO_x = NO_2 + NO$, parts per million

Emission Index Calculations

1. Carbon monoxide emission index, $\mathrm{lbm_{CO}}/1000\ \mathrm{lb_{fuel}}$

$$\mathrm{EI[CO]} = \frac{P5}{EM} \times \frac{1000 \times MWCO}{MWC + ALPHA \times MWH}$$

2. Unburned hydrocarbons emission index, $\mathrm{lbm_{HC}}/1000\ \mathrm{lb_{fuel}}$

$$\mathrm{EI[HC]} = \frac{EM \times P6}{EM} \times \frac{1000 \times \left(MWC \times EM + MWH \times EN \right)}{MWC + ALPHA \times MWH}$$

3. Combustion efficiency

$$\mathrm{ETAb} = \left(1.0 - 4.346 \times \frac{EI[CO]}{FLHV} - \frac{EI[HC]}{1000}\right) \times 100$$

Calculation Of Adiabatic Flame Temperature

1. Percent fuel flow, moles of fuel per total moles of fuel and air

$$WFP = \frac{WFTM}{WFTM + WAIRM}$$

2. Percent air flow, moles of air per total moles of fuel and air

$$WAP = \frac{WAIRM}{WFTM + WAIRM}$$

3. Adjusted number of moles of fuel required to conserve mass, moles of fuel

$$WFMADJ = PT \times WFP$$

4. Adjusted number of moles of air required to conserve mass, moles of air

$$WAMADJ = PT \times WAP$$

5. Temperature of fuel and air in combustion process, °K

$$TG06K = \frac{(TG06 + 460)}{1.8}$$

6. Heat of formation of the products minus the reactants, cal

$$HF = P1 \times HFCO2 + P5 \times HFCO + P8 \times HFNO + P4 \times HFH2O + (P6 - WFMADJ) \times ENTHALPY$$

7. Enthalpy of the products minus the reactants at 298 °K, cal

$$H0 = (WFMADJ - P6) \times DHCH4 + (0.21 \times WAMADJ - P3) \times DHO2 + (0.79 \times WAMADJ - P2) \times DHN2 - P1 \times DHCO2 - P5 \times DHCO - P8 \times DHNO - P4 \times DHH2O$$

8. Enthalpy of the reactants at the combustor inlet temperature, cal

$$HR = -WFMADJ \times (M6 \times TG06K - B6) - 0.21 \times WAMADJ \times (M3 \times TG06K - B3) - 0.79 \times WAMADJ \times (M2 \times TG06K - B2)$$

9. Sum of curve fit intercepts for products at the flame temperature, cal

$$BTF = P2 \times B2 + P3 \times B3 + P1 \times B1 + P5 \times B5 + P8 \times B8 + P4 \times B4 + P6 \times B6$$

10. Sum of curve fit slopes for products at the flame temperature, cal

$$MTF = P2 \times M2 + P3 \times M3 + P1 \times M1 + P5 \times M5 + P8 \times M8 + P4 \times M4 + P6 \times M6$$

11. Adiabatic flame temperature, °K

$$TFK = \frac{(HF + HO + HR + BTF)}{MTF}$$

12. Adiabatic flame temperature, °R

$$TFR = TFK \times 1.8$$

13. Adiabatic flame temperature, °F

$$TFF = TFR - 460$$

<u>Combustor Performance Analysis</u>

1. Exhaust gas ratio of specific heat, cal/mole-°K

$$CPK = \begin{pmatrix} (TFK \times M1 + B1) \times MWCO2 + (TFK \times M2 + B2) \times 2 \times MWN + \\ (TFK \times M3 + B3) \times 2 \times MWO + (TFK \times M4 + B4) \times MWH2O + \\ (TFK \times M5 + B5) \times MWCO + (TFK \times M6 + B6) \times MWCH4 + \\ (TFK \times M8 + B8) \times MWNO \end{pmatrix} \div TFK$$

2. Exhaust gas ratio of specific heat, BTU/lbm-°R

$$CPR = \frac{CPK \times 4.186}{1055 \times MW}$$

3. Ratio of specific heats

$$GAMMA = \frac{CPR \times 778}{CPR \times 778 - RGC}$$

4. Combustor exit Mach number

$$M12 = \left(\left(\left(\frac{PT12}{PS12}\right)^{\left(\frac{GAMMA-1}{GAMMA}\right)} - 1\right) \times \frac{2}{(GAMMA-1)}\right)^{0.5}$$

5. Combustor exit total temperature, °F

$$TT12 = \left(TFR \times \left(1 + \frac{GAMMA-1}{2} \times M12^2\right)\right) - 460$$

6. Total mass flow at the combustor exit, lbm/sec

$$MDOT12 = WFT + WAIR$$

7. Velocity at combustor exit, ft/sec

$$V12 = (GAMMA \times RGC \times GC \times TFR)^{0.5} \times M12$$

APPENDIX C

Slot Wall Heating Calculation

The heat transfer to the probe surface inside the slot is required in the probe cooling calculations. The side walls of the slot were modeled as two flat plates 0.88 inches in length. The Mach number in the slot is 0.47 and the Reynolds number is 3.72×10^{5}. Fully turbulent flow was assumed over the entire length of the slot. Due to the small surface area and limited view factor, radiation and gaseous emission heating is considered negligible. Due to the complex flow over the top and bottom of the slot, the heat flux in these areas is unknown.

1. Prandtl number is nearly constant over the temperature range from 1500 to 3500 °R

$$Pr = 0.713$$

2. The Nusselt number is calculated from the Chilton-Colburn analogy [11]

$$N_x = 0.0296 \times Re_x^{\frac{4}{5}} \times Pr^{\frac{1}{3}} = 756.5$$

3. The film coefficient is

$$\bar{h} = \frac{\overline{Nu_x} \times k}{L} = 0.192 \frac{BTU}{ft^2 - s - {}^{\circ}R}$$

4. The slot wall is maintained at 1660 °R so the convective heating load into each slot wall is

$$\bar{q} = \bar{h} \times A_{wall} \times \left(T_{wall} - T_{gas}\right) = 2.99 \frac{BTU}{sec}$$

APPENDIX D

Summary of Hydraulic Calculations

The method of calculations contained in this Appendix was used to determine the water flow distribution through each of the machined flow paths in the probe and the total pressure loss across the probe for a range of water supply pressures. Given the probe design surface temperature of 1200 °F and the total heating load on the probe surface, the cooling efficiency of each flow path was calculated.

1. Probe diameter, in

$$PROBED = 0.94$$

2. Probe length, in

$$PROBEL = 4.8$$

3. Probe design surface temperature, °F

$$TSURF = 1200$$

4. Facility water supply pressure estimated to range from 300 to 600 psia

$$300 \le PS \le 600$$

5. Maximum facility water system back pressure, psia

$$PB = 100$$

6. Facility water supply temperature, °F

$$TS = 70$$

7. Gravitational acceleration, ft/sec^2

$$GC = 32.174$$

8. Specific weight of water, lbm/ft^3

$$SW = 62.3$$

9. Specific heat of water, BTU/lbm-R

$$CPW = 1.0012$$

10. Water dynamic viscosity at TS, lbf-s/ft^2

$$MUW = 8E^{-7} \times TS^{-1.1535}$$

11. Water thermal conductivity at TS, lbf-s/ft^2

$$KW = 0.226 \times TS^{0.1032}$$

12. Water Prandtl number at TS

$$PRW = 1387.3 \times TS^{-1.2468}$$

13. Cooling water flow rate for a given facility water supply pressure obtained from flow characteristics of a similar probe design, gpm

$$MDOTW = (PS - PB)^{\frac{1}{2}} \times 0.1456 - 0.2829$$

14. DFX - diameter of facility water supply / return tube "X", ft.

15. LFX - length of facility water supply / return tube "X", ft.

16. AFX - area of facility water supply / return tube "X", ft^2

17. Velocity in facility water supply / return tube "X", ft/sec

$$VFX = \frac{MDOTW}{SW \times AFX}$$

18. Reynolds number in facility water supply / return tube "X"

$$REFX = \frac{SW \times VFX \times DFX}{MUW \times GC}$$

19. Friction factor for facility water supply / return tube "X"

$$FFX = \left(1.82 \times \log REFX - 1.64\right)^{-2}$$

20. Head loss for facility supply / return tube "X", ft.

$$HFX = \frac{FFX \times LFX}{DFX \times VFX^2 \times 2 \times GC}$$

21. Total head loss in facility water supply tubing, ft

$$HFST = HFA + HFB$$

22. Total head loss in facility water return tubing, ft.

$$HFRT = HFC + HFD$$

23. Water pressure in probe supply manifold, psia

$$PSM = PS - \frac{HFST \times SW}{144}$$

24. Minimum water pressure required in probe return manifold, psia

$$PRM = PB + \frac{HFRT \times SW}{144}$$

25. Water supply manifold area, ft^2

$$ASM = 1.01E^{-3}$$

26. Water turn around manifold area, ft^2

$$ATM = 9.26E^{-4}$$

27. Water return manifold area, ft^2

$$ARM = 1.01E^{-3}$$

28. Water supply manifold velocity, ft/sec

$$VSM = \frac{MDOTW}{SW \times ASM}$$

29. Water turn around manifold velocity, ft/sec

$$VTM = \frac{MDOTW}{SW \times ATM}$$

30. Water return manifold velocity, ft/sec

$$VRM = \frac{MDOTW}{SW \times ARM}$$

31. DX - diameter of flow path "X", in.

32. LX - length of flow path "X", in.

33. AX - cross sectional area of flow path "X", ft^2

34. Flow path wetted surface area, ft^2

$$PX = \frac{DX \times LX \times \pi}{144}$$

35. SEGX - probe surface segment above each flow path "X", deg. (see Figure 11)

36. LMX - maximum metal path length from the surface to the cooling water, in. (see Figure 11)

37. Probe surface area above each flow path, ft^2

$$ASURFX = \frac{PROBED \times SEGX \times \pi \times PROBEL}{2 \times 180 \times 144}$$

Flow Path	Diameter, in	Length, in	Cross Sectional Area, ft^2	Wetted Area, ft^2	Arc Segment Above Flow Path, deg	Surface Area Above Flow Path, ft^2	Maximum Metal Distance to Surface, in
A	0.03	5.94	4.9E-6	3.89E-3	15	4.10E-3	0.078
B	0.03	5.94	4.9E-6	3.89E-3	13	3.56E-3	0.078
C	0.059	5.94	1.9E-5	7.65E-3	21	5.74E-3	0.085
D	0.059	5.94	1.9E-5	7.65E-3	21	5.74E-3	0.095
E	0.059	6.5	1.9E-5	8.37E-3	20	5.47E-3	0.095
F	0.059	6.5	1.9E-5	8.37E-3	20	5.47E-3	0.095
G	0.059	5.94	1.9E-5	7.65E-3	21	5.74E-3	0.095
H	0.059	5.94	1.9E-5	7.65E-3	21	5.74E-3	0.085
I	0.03	5.94	4.9E-6	3.89E-3	13	3.56E-3	0.078
J	0.03	5.94	4.9E-6	3.89E-3	15	4.10E-3	0.078

38. MDOT1X - water mass flow rate through supply flow path “X”, lbm/sec

MDOT1X = The mass flow rate through each flow path is adjusted until MDOTST = MDOTW and PTM is the same for each flow path.

39. Total supply water flow rate, lbm/sec

$$MDOTST = MDOT1A + MDOT1B + MDOT1C + MDOT1E + MDOT1F + MDOT1G + MDOT1H + MDOT1I + MDOT1J$$

40. Water velocity through supply flow path “X”, ft/sec

$$V1X = \frac{MDOT1X}{SW \times AX}$$

41. Water flow Reynolds number through supply flow path “X”

$$RE1X = \frac{SW \times V1X \times DX}{MUW \times GC \times 12}$$

42. Friction factor for supply flow path "X"

$$F1X = \left(1.82 \times \log RE1X - 1.64\right)^{-2}$$ (Daugherty and Franzini, [15])

43. Friction loss for supply flow path "X", ft

$$HF1X = \frac{F1X \times LSX}{DX \times V1X^2 \times 2 \times GC}$$

44. Entrance loss factor for supply flow path "X"

KE1X = f(DX/local manifold diameter, D1X) (Daugherty and Franzini, [15])

Flow path	(DX/D1X)	KE1X
A,B,I,J	0.476	0.337
C,H	0.453	0.344
D,G	0.320	0.382
E,F	0.236	0.409

45. Entrance loss for supply flow path "X", ft

$$HE1X = \frac{KE1X \times V1X^2}{2 \times GC}$$

46. Four - elbow loss factor for supply flow path "X"

$KL2X = 0.9$ for short radius elbow (Daugherty and Franzini, [15])

47. Four - elbow loss for supply flow path "X", ft

$$HL2X = \frac{KL2X \times V1X^2}{2 \times GC}$$

48. Sudden expansion loss for supply flow path "X", ft

$$HX3X = \frac{(V1X - VTM)^2}{2 \times GC}$$

49. Water pressure in the turn around manifold, psia

$$PTM = \frac{PSM \times 144}{SW} + \frac{V1X^2 - VTM^2}{2 \times GC} + \frac{(HF1X + HE1X + HL2E + HX3X) \times SW}{144}$$

50. MDOT4X - water mass flow rate through return flow path "X", lbm/sec

MDOT4X = The mass flow rate through each flow path is adjusted until MDOTRT = MDOTW and PRM is the same for each flow path.

51. Total return water flow rate, lbm/sec

$$MDOTRT = MDOT4A + MDOT4B + MDOT4C + MDOT4E + MDOT4F + MDOT4G + MDOT4H + MDOT4I + MDOT4J$$

52. Water velocity through return flow path "X", ft/sec

$$V4X = \frac{MDOT4X}{SW \times AX}$$

53. Water flow Reynolds number through return flow path "X"

$$RE4X = \frac{SW \times V4X \times DX}{MUW \times GC \times 12}$$

54. Friction factor for return flow path "X"

$$F4X = (1.82 \times \log RE4X - 1.64)^{-2}$$ (Incropera and DeWitt, [11])

55. Friction loss for return flow path "X", ft

$$HF4X = \frac{F4X \times LX}{DX \times V4X^2 \times 2 \times GC}$$

56. Entrance loss factor for return flow path "X"

KE4X = f (DX/local manifold diameter, D4X) (Daugherty and Franzini, [15])

Flow path	(DX/D4X)	KE4X
A	0.137	0.482
B	0.137	0.482
C	0.269	0.399
D	0.315	0.386
E	0.378	0.367
F	0.472	0.338
G	0.628	0.263
H	1.269	0
I	1.0	0
J	1.0	0

57. Entrance loss for return flow path "X", ft

$$HE4X = \frac{KE4X \times V4X^2}{2 \times GC}$$

58. Four - elbow loss factor for return flow path "X"

$KL5X = 0.9$ for short radius elbow (Daugherty and Franzini, [15])

59. Four - elbow loss for return flow path "X", ft

$$HL5X = \frac{KL5X \times V4X^2}{2 \times GC}$$

60. Sudden expansion loss for return flow path "X", ft

$$HX6X = \frac{(V4X - VRM)^2}{2 \times GC}$$

61. Water pressure in the return manifold, psia

$$PRM = \frac{PTM \times 144}{SW} + \frac{VTM^2 - VRM^2}{2 \times GC} + \frac{(HF4X + HE4X + HL5E + HX6X) \times SW}{144}$$

62. Total pressure loss across the probe, psia

$$DELP = PSM - PRM$$

63. Prandtl number of the return water at TS

$$PRW = 1387.3 \times TS^{-1.2468}$$

64. Local Nusselt number for supply flow path "X"

$$NU1X = 0.023 \times RE1X^{0.8} PRW^{0.4}$$

65. Water thermal conductivity at TS, BTU/ft-hr-°R

$$KW = 0.226 \times TS^{0.1032}$$

66. Water film coefficient for supply flow path "X", BTU/hr-ft^2-°F

$$HW1X = \frac{NU1X \times KWS \times 12}{DX}$$

67. QDOTFPX - total heat load to the surface area segment above flow path "X" from heat load analysis, BTU/sec

68. Thermal conductivity of AISI 304 stainless steel at TSURF, BTU/ft-s-°F

$$KSSTL = 0.0046 \times TSURF + 8.4213$$

69. Wall temperature of supply flow path "X", °F

$$TFPWALLX = \frac{\left(\frac{KSSTL \times ASURFX \times TSURF \times 12}{LMX} + HW1X \times PX \times TS\right)}{\frac{KSSTL \times ASURFX \times 12}{LMX} + HW1X \times PX}$$

70. Bulk water temperature at the exit of supply flow path "X", °F

$$TFPWATERX = \frac{QDOTFPX}{MDOT1X \times CPW} + TS$$

71. Water temperature in the turn around manifold, °F

$$TTM = \frac{\sum_{A}^{J}(MDOTPX \times TFPWATERX)}{(MDOTW)}$$

72. Prandtl number for water at TTM

$$PRW = 1387.3 \times TTM^{-1.2468}$$

73. Local Nusselt number for return flow path "X"

$$NU4X = 0.023 \times RE4X^{0.8} PRW^{0.4}$$

74. Water thermal conductivity at TTM, BTU/ft-hr-°R

$$KW = 0.226 \times TTM^{0.1032}$$

75. Water film coefficient for return flow path "X", BTU/hr-ft^2-F

$$HW4X = \frac{NU4X \times KWR \times 12}{DX}$$

76. Wall temperature of return flow path "X", °F

$$TFPWALLX = \frac{\left(\frac{KSSTL \times ASURFX \times TSURF \times 12}{LMX} + HW4X \times PX \times TTM\right)}{\frac{KSSTL \times ASURFX \times 12}{LMX} + HW4X \times PX}$$

77. Bulk water temperature at the exit of return flow path "X", °F

$$TFPWATERX = \frac{QDOTFP}{MDOT4X \times CPW} + TTM$$

78. Water temperature in the return manifold, °F

$$TR = \frac{\sum_{A}^{J}(MDOTPX \times TFPWATERX)}{(MDOTW)}$$

79. Total temperature rise across the probe, °F

$$DELT = TR - TS$$

Hybrid Probe Hydraulic Analysis										
Water Supply Pressure, PS =	600	psia		Pressure Loss in Probe Water Supply and Return Tubing						
Water Flow Rate, MDOTW =	2.97	gpm		DFX,ft	AFX, ft^2	LFX, ft	VFX, ft/sec	REFX	FFX	HFX,ft
Water Flow Rate, MDOTW =	0.414	lbm/sec	Supply A	0.036	0.0010	34	6.569	2.13E+04	0.0257	16.36
Water Pressure in Supply Manifold, PSM =	566.5	psia	Supply B	0.018	0.0003	4.7	26.275	4.25E+04	0.0217	61.15
Min.Pressure in Return Manifold, PRM =	131.1	psia	Return B	0.018	0.0003	4.7	26.275	5.85E+04	0.0202	56.85
Water Back Pressure, PB =	100	psia	Return A	0.036	0.0010	34	6.569	2.92E+04	0.0238	15.11
Water Supply Temperature, TS =	70	F								
Water Viscosity, MUW, at TS =	2.14E-05	lbf-s/ft^2		Supply Manifold Velocity, VSM =			6.554	ft/sec		
Water Return Temperature, TTM =	92.2	F		Turnaround Manifold Velocity, VTM =			7.170	ft/sec		
Water Viscosity, MUW, at TTM =	1.56E-05	lbf-s/ft^2		Return Manifold Velocity, VRM =			6.554	ft/sec		
Supply Manifold Flow Area, ASM =	1.01E-03	ft^2		Water Specific Weight, SW =			62.3	lb/ft^3		
Turnaround Manifold Flow Area, ATM =	9.26E-04	ft^2								
Return Manifold Flow Area, ARM =	1.01E-03	ft^2								

			Station 1-3	Station 1	Station 1	Stations 1-3			Station 1	Station 2	Station 3	Station 3-4	Station 3-4
Flow Path	Dia., in.	Area,ft^2	Mass Flow Through Supply Flow Path, lbm/sec	Supply Flow Path Entrance Velocity, ft/sec	Supply Flow Path Reynolds Number	Flow Path Length, in.	Friction Factor (Moody Diagram)	Supply Flow Path Friction Loss, ft	Supply Flow Path Entrance Loss, ft	Elbow Loss, ft	Turn Around Manifold Sudden Expansion Loss, ft	Turnaround Manifold Velocity, ft/sec	Turnaround Manifold Pressure, psia
	DX	AX	MDOT1X	V1X	RE1X	LX	F1X	HF1X	HE1X	HL2X	HX3X	VTM	PTM
A	0.0300	4.9E-06	0.0122	39.87	9.00E+03	5.940	0.0324	158.38	8.32	0	16.62	7.17	487.1
B	0.0300	4.9E-06	0.0122	39.87	9.00E+03	5.940	0.0324	158.38	8.32	0	16.62	7.17	487.1
C	0.0590	1.9E-05	0.0679	57.37	2.55E+04	5.940	0.0246	126.55	17.60	0	39.17	7.17	487.1
D	0.0590	1.9E-05	0.0675	57.05	2.53E+04	5.940	0.0246	125.32	19.32	0	38.67	7.17	487.1
E	0.0590	1.9E-05	0.0464	39.25	1.74E+04	6.500	0.0271	71.36	9.79	86.17682	15.99	7.17	487.1
F	0.0590	1.9E-05	0.0464	39.25	1.74E+04	6.500	0.0271	71.36	9.79	86.17682	15.99	7.17	487.1
G	0.0590	1.9E-05	0.0675	57.05	2.53E+04	5.940	0.0246	125.32	19.32	0	38.67	7.17	487.1
H	0.0590	1.9E-05	0.0679	57.37	2.55E+04	5.940	0.0246	126.55	17.60	0	39.17	7.17	487.1
I	0.0300	4.9E-06	0.0122	39.87	9.00E+03	5.940	0.0324	158.38	8.32	0	16.62	7.17	487.1
J	0.0300	4.9E-06	0.0122	39.87	9.00E+03	5.940	0.0324	158.38	8.32	0	16.62	7.17	487.1
Total Flow Rate, lbm/sec =			0.4123						Average Turn Around Manifold Pressure =				487.1
Target Flow Rate, lbm/sec =			0.4136									STDD =	0.00
Percent Difference =			-0.30										

Figure D1. Typical Hydraulic Calculations

Hybrid Probe Hydraulic Analysis

Water Supply Pressure, PS =	600	psia		Pressure Loss in Probe Water Supply and Return Tubing						
Water Flow Rate, MDOTW =	2.97	gpm		DFX,ft	AFX, ft^2	LFX, ft	VFX, $^{ft}/_{sec}$	REFX	FFX	HFX,ft
Water Flow Rate, MDOTW =	0.414	lbm/sec	Supply A	0.036	0.0010	34	6.569	2.13E+04	0.0257	16.36
Water Pressure in Supply Manifold, PSM =	566.5	psia	Supply B	0.018	0.0003	4.7	26.275	4.25E+04	0.0217	61.15
Min.Pressure in Return Manifold, PRM =	131.1	psia	Return B	0.018	0.0003	4.7	26.275	5.85E+04	0.0202	56.85
Water Back Pressure, PB =	100	psia	Return A	0.036	0.0010	34	6.569	2.92E+04	0.0238	15.11
Water Supply Temperature, TS =	70	F								
Water Viscosity, MUW, at TS =	2.14E-05	lbf-s/ft^2		Supply Manifold Velocity, VSM =			6.554	ft/sec		
Water Return Temperature, TTM =	92.2	F		Turnaround Manifold Velocity, VTM =			7.170	ft/sec		
Water Viscosity, MUW, at TTM =	1.56E-05	lbf-s/ft^2		Return Manifold Velocity, VRM =			6.554	ft/sec		
Supply Manifold Flow Area, ASM =	1.01E-03	ft^2		Water Specific Weight, SW =			62.3	lb/ft^3		
Turnaround Manifold Flow Area, ATM =	9.26E-04	ft^2								
Return Manifold Flow Area, ARM =	1.01E-03	ft^2								

Station 4-6	Station 4	Station 4	Stations 4-6		Station 4	Station 5	Station 6	Station 6	Station 6
Mass Flow Through Return Flow Path, lbm/sec	Return Flow Path Entrance Velocity, ft/sec	Return Flow Path Reynolds Number	Friction Factor (Moody Diagram)	Return Flow Path Friction Loss, ft	Return Flow Path Entrance Loss, ft	Elbow Loss, ft	Return Manifold Sudden Expansion Loss, ft	Return Manifold Velocity, ft/sec	Return Manifold Pressure, psia
MDOT4X	V4X	RE4X	F4X	HF4X	HE4X	HL5X	HX6X	VRM	PRM
0.0121	39.53	1.23E+04	0.0297	142.81	11.70	0	16.90	6.55	412.7
0.0121	39.53	1.23E+04	0.0297	142.81	11.70	0	16.90	6.55	412.7
0.0666	56.30	3.44E+04	0.0228	113.30	19.65	0	38.46	6.55	412.7
0.0667	56.41	3.44E+04	0.0228	113.69	19.09	0	38.63	6.55	412.7
0.0456	38.56	2.36E+04	0.0251	63.81	8.48	83.20	15.92	6.55	412.7
0.0457	38.64	2.36E+04	0.0250	64.03	7.84	83.54	16.00	6.55	412.7
0.0680	57.50	3.51E+04	0.0227	117.57	13.51	0	40.33	6.55	412.7
0.0710	60.05	3.67E+04	0.0225	126.94	0.00	0	44.48	6.55	412.7
0.0126	41.11	1.28E+04	0.0294	152.85	0.00	0	18.56	6.55	412.7
0.0126	41.11	1.28E+04	0.0294	152.85	0.00	0	18.56	6.55	412.7
0.4130	=Total Flow Rate, lbm/sec				Average Return Manifold Pressure =				412.7
0.4136	=Target Flow Rate, lbm/sec						Standard Deviation =		0.00
-0.14	=Percent Difference								

Figure D1. Typical Hydraulic Calculations (Concluded)

ProbeCooling Analysis			
Probe Surface Temperature, TSURF =	1200	F =	1660 R
Stainless Steel Thermal Conductivity at TS, KSSTL =	13.94	$^{BTU}/hr\text{-}ft\text{-}F$	
Cooling Water Flow Rate, MDOTW =	2.97	gpm =	0.414 lbm/sec
Cooling Water Supply Pressure, PS =	600	psia	
Cooling Water Back Pressure, PB =	100	psia	
Water Specific Weight, SW =	62.3	lb/ft^3	
	TS	TTM	
Cooling Water Temperature, F =	70	92.2	
Water Viscosity, MU, $^{lbf\text{-}s}/ft^2$ =	2.14E-05	1.56E-05	
Water Thermal Conductivity, KW, $^{BTU}/ft\text{-}hr\text{-}R$ =	0.341	0.351	
Water Prandtl Number, PRW =	6.945	4.924	

Flow Path	Flow Path Dia., in	Flow Path Cross Sectional Area, ft^2	Flow Path Length, in	Flow Path Surface Area, ft^2	Probe Surface Segment Above Flow Flow Path, deg	Probe Surface Area Above Flow Flow Path, ft^2	Max Metal Path Length, in	Mass Flow Through Flow Path, lbm/sec	Flow Path Reynolds Number	Water Nusselt Number	Water Film Coefficient, $^{BTU}/hr\text{-}ft^2\text{-}F$	Total Heat Flux To Metal Above Flow Path, $^{BTU}/_{sec}$	Flow Path Wall Temperature, F	Bulk Water Temperature at Flow Path Exit, F
Supply	DX	AX	LX	PX	SEGMENT	AS	LM	MDOT1X	RE1X	NU1X	HW1X	QDOTFP	TFPWALL	TFPWATER
A	0.03	4.91E-06	5.94	3.888E-03	75 - 90	4.102E-03	0.078	0.0122	9.00E+03	72.78	68.95	0.580	1166.6	117.4
B	0.03	4.91E-06	5.94	3.888E-03	62 - 75	3.555E-03	0.078	0.0122	9.00E+03	72.78	68.95	0.617	1161.6	120.4
C	0.059	1.9E-05	5.94	7.646E-03	41 - 62	5.742E-03	0.085	0.0679	2.55E+04	167.28	80.58	1.117	1141.6	86.4
D	0.059	1.9E-05	5.94	7.646E-03	20 - 41	5.742E-03	0.095	0.0675	2.53E+04	166.54	80.23	1.184	1135.4	87.5
E	0.059	1.9E-05	6.5	8.367E-03	0 - 20	5.469E-03	0.095	0.0464	1.74E+04	123.46	59.47	1.162	1144.5	94.9
F	0.059	1.9E-05	6.5	8.367E-03	340 - 0	5.469E-03	0.095	0.0464	1.74E+04	123.46	59.47	1.162	1144.5	94.9
G	0.059	1.9E-05	5.94	7.646E-03	319 - 340	5.742E-03	0.095	0.0675	2.53E+04	166.54	80.23	1.184	1135.4	87.5
H	0.059	1.9E-05	5.94	7.646E-03	298 319	5.742E-03	0.085	0.0679	2.55E+04	167.28	80.58	1.117	1141.6	86.4
I	0.03	4.91E-06	5.94	3.888E-03	285 - 298	3.555E-03	0.078	0.0122	9.00E+03	72.78	68.95	0.617	1161.6	120.4
J	0.03	4.91E-06	5.94	3.888E-03	270 - 285	4.102E-03	0.078	0.0122	9.00E+03	72.78	68.95	0.580	1166.6	117.4
										Bulk water temperature in turn-around manifold, TTM =				92.2
Return	DX	AX	LX	PX	SEGMENT	AS	LM	MDOT4X	RE4X	NU4X	HW4X	QDOTFP	TFPWALL	TFPWATER
A	0.03	4.91E-06	5.94	3.888E-03	90 - 105	4.102E-03	0.078	0.0121	1.23E+04	81.25	76.98	0.761	1162.8	155.0
B	0.03	4.91E-06	5.94	3.888E-03	105 - 118	3.555E-03	0.078	0.0121	1.23E+04	81.25	76.98	0.914	1157.3	167.6
C	0.059	1.9E-05	5.94	7.646E-03	118 - 139	5.742E-03	0.085	0.0666	3.44E+04	185.23	89.23	1.236	1135.7	110.7
D	0.059	1.9E-05	5.94	7.646E-03	139 - 160	5.742E-03	0.095	0.0667	3.44E+04	185.52	89.37	1.147	1128.5	109.4
E	0.059	1.9E-05	6.5	8.367E-03	160 - 180	5.469E-03	0.095	0.0456	2.36E+04	136.85	65.92	1.243	1138.8	119.4
F	0.059	1.9E-05	6.5	8.367E-03	180 - 200	5.469E-03	0.095	0.0457	2.36E+04	137.07	66.03	1.243	1138.7	119.3
G	0.059	1.9E-05	5.94	7.646E-03	200 - 221	5.742E-03	0.095	0.0680	3.51E+04	188.37	90.74	1.147	1127.4	109.1
H	0.059	1.9E-05	5.94	7.646E-03	221 - 242	5.742E-03	0.085	0.0710	3.67E+04	195.04	93.96	1.236	1132.5	109.6
I	0.03	4.91E-06	5.94	3.888E-03	242 - 255	3.555E-03	0.078	0.0126	1.28E+04	83.85	79.44	0.914	1156.0	164.7
J	0.03	4.91E-06	5.94	3.888E-03	255 - 270	4.102E-03	0.078	0.0126	1.28E+04	83.85	79.44	0.761	1161.7	152.6
										Bulk water temperature in return manifold, TR =				117.7

Figure D2. Typical Cooling Calculations

APPENDIX E

Derivation of the One - Dimensional

Heat Transfer Model

Referring to Figure 11, a one - dimensional heat transfer model was constructed to calculate the wall temperatures of each cooling water flow path. The difference in the flow path wall temperatures across the probe were used to estimate the thermal deformation and misalignment of the optical components. The one - dimensional model is derived below.

1. The total heat load to the probe surface segment ASURFX above each cooling water flow path "X" from the heating load calculations, BTU/sec.

$$QDOTFPX = \overline{q_{convection}} + \overline{q_{radiation}} + \overline{q_{emission}}$$

2. The steady state heat transfer from the probe surface to the cooling water, BTU/sec.

$$QDOTFPX = \frac{k \times ASURX}{LMX} \times \left(T_{SURF} - T_{WALL}\right) = h_{WATER} \times PX \times \left(T_{WALL} - T_{WATER}\right)$$

3. The heat added to the cooling water is derived from an energy balance of the cooling water system where $T_{WATER\ INLET}$ is specified, BTU/sec

$$QDOTFPX = MDOTX \times Cp_{WATER} \times \left(T_{WATER} - T_{\substack{WATER \\ INLET}}\right)$$

4. Equation 3. is solved for T_{water}, °R.

$$T_{WATER} = \frac{QDOTFPX}{MDOTX \times Cp_{WATER}} + T_{\substack{INLET \\ WATER}}$$

5. The right part of Equation 2. is solved for T_{WALL}, °R

6. $$T_{WALL} = \frac{\dfrac{k \times ASURFX \times T_{SURF}}{LMX} + h_{WATER} \times PX \times T_{WATER}}{h_{WATER} \times PX + \dfrac{k \times ASURFX}{LMX}}$$

VITA

Paul Armand Jalbert was born on May 9, 1954 in Worcester, MA to Armand W. and Theresa G. Jalbert of Spencer, MA. He graduated from East Catholic High School in Manchester, CT in 1972 and Parks College of St. Louis University in Cahokia, IL with a Bachelor of Science degree in Aerospace Engineering in 1976. Paul accepted employment with ARO, Inc. at the Arnold Engineering Development Center at Arnold Air Force Base, TN in May, 1976. During his twenty-one year engineering career with ARO, Inc. (now called Sverdrup Technology, Inc., AEDC Group) Paul worked as an engineer and project manager in supersonic wind tunnel testing, solid and liquid rocket testing, and instrumentation system development for aircraft turbine engine testing.

Paul is married to Cynthia A. Jalbert and they have one son, Stephen. The Jalberts reside in Lynchburg, TN.